https://lib.uliege.be https://matheo.uliege.be

Mémoire

Auteur : Gilon, Charles-Antoine
Promoteur(s) : Rauw, Grégor; Nazé, Yaël
Faculté : Faculté des Sciences
Diplôme : Master en sciences spatiales, à finalité approfondie
Année académique : 2024-2025
URI/URL : http://hdl.handle.net/2268.2/22965

Avertissement à l'attention des usagers :

Tous les documents placés en accès ouvert sur le site le site MatheO sont protégés par le droit d'auteur. Conformément aux principes énoncés par la "Budapest Open Access Initiative"(BOAI, 2002), l'utilisateur du site peut lire, télécharger, copier, transmettre, imprimer, chercher ou faire un lien vers le texte intégral de ces documents, les disséquer pour les indexer, s'en servir de données pour un logiciel, ou s'en servir à toute autre fin légale (ou prévue par la réglementation relative au droit d'auteur). Toute utilisation du document à des fins commerciales est strictement interdite.

Par ailleurs, l'utilisateur s'engage à respecter les droits moraux de l'auteur, principalement le droit à l'intégrité de l'oeuvre et le droit de paternité et ce dans toute utilisation que l'utilisateur entreprend. Ainsi, à titre d'exemple, lorsqu'il reproduira un document par extrait ou dans son intégralité, l'utilisateur citera de manière complète les sources telles que mentionnées ci-dessus. Toute utilisation non explicitement autorisée ci-avant (telle que par exemple, la modification du document ou son résumé) nécessite l'autorisation préalable et expresse des auteurs ou de leurs ayants droit.

A photometric and spectroscopic study of the variability of the O7.5 supergiant HD192639

Author: Charles-Antoine Gilon
Supervisors: Gregor Rauw, Yaël Nazé
2024-2025

A Master thesis presented in partial fulfillment of the requirements
for the Degree of Master in Space Sciences

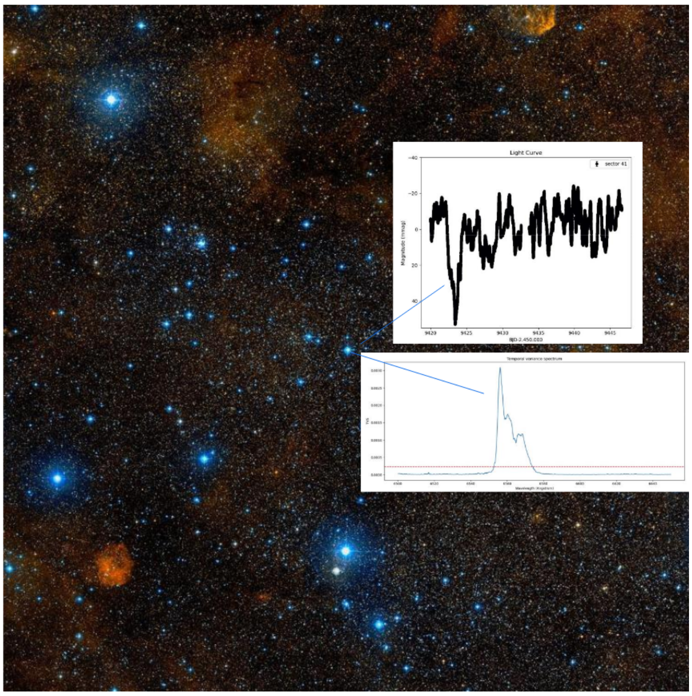

LIÈGE université
Sciences

Acknowledgements

I would like to express my deepest gratitude to my mentors, Dr. Gregor Rauw and Dr. Yaël Nazé. Their guidance, encouragement, and unwavering support were invaluable throughout this work. Dr. Rauw's analytical precision and insightful feedback helped me strengthen the foundation of my research, while Dr. Nazé's enthusiasm and clarity were a constant source of motivation and inspiration. During moments of doubt or overwhelm, both were patient and generous with their time, and their belief in my abilities helped me stay focused and resilient.

Their mentorship went beyond this thesis—they taught me how to approach scientific questions with curiosity, how to think critically, and how to communicate effectively as a scientist. I will carry these lessons with me throughout my career.

I would also like to extend my heartfelt thanks to my parents and my girlfriend. Their constant emotional support, understanding, and encouragement were essential throughout this journey. Their belief in me, especially during the more difficult moments, gave me the strength to persevere.

Finally, I am grateful to my peers and colleagues, and in particular, Maria Groyne, whose insightful discussions and camaraderie enriched this experience.

Abstract

This thesis investigates the photometric and spectroscopic variability of the O7.5 Iabf-type supergiant star HD 192639, utilizing data from TESS and the TIGRE telescope. Previous studies identified a potential 4.76-day period in the stellar wind variability, potentially linked to large-scale structures or magnetic activity. This work aims to confirm or refute this period using new observational datasets, including simultaneous photometric and spectroscopic data, a first for this object. Fourier analysis and Temporal Variance Spectra (TVS) reveal no statistically significant persistent periodicity in the TESS light curves, though a marginal signal consistent with the 4.76-day timescale appears repeatedly in both photometry and spectroscopy. Spectroscopic analysis confirms significant variability in several wind-sensitive lines (notably He II 4686, Hβ, He I 5876, and Hα) consistent with large-scale wind structures. However, TVS for photospheric lines such as He II 4200 only show stochastic variations. Radial velocity measurements, performed on photospheric spectral lines, yield no evidence for binarity. Hence, the observed variability is most likely intrinsic to the O7.5 supergiant and does not arise from binary interactions. Although the variations of HD 192639 are clearly not strictly periodic, our results support the idea that the 4.76-day timescale reflects a stable clock, most probably associated with the stellar rotation. Localized magnetic fields, leading to bright spots, are likely at the origin of the large-scale wind structures. A very special behaviour was observed during the night of July 27–28, 2021: wind-sensitive spectral lines displayed a blueward shifting narrow absorption component. This coincides with an anomalously strong photometric dip, suggesting an episodic enhanced mass ejection event. Overall, these findings refine our understanding of HD 192639's wind structure and variability, and underline the added value of long-term, high-cadence monitoring to unravel the dynamics of massive star winds.

Table of Contents

1 Introduction **4**
- 1.1 Massive stars in the context of modern astrophysics . . . 4
- 1.2 The variability of massive stars . . . 5
- 1.3 Classification of HD 192639 . . . 6
- 1.4 Observational History and Previous Results . . . 7
- 1.5 Possible Origins of Stellar Wind Variability . . . 8
- 1.6 Purpose of this work . . . 10
- 1.7 Brief overview of this work . . . 10

2 Instruments **12**
- 2.1 TESS . . . 12
  - 2.1.1 The TESS Mission Design . . . 12
  - 2.1.2 Scientific Instruments and Technical Specificities . . . 13
  - 2.1.3 The Data Processing . . . 14
  - 2.1.4 Limitations . . . 16
- 2.2 Tigre . . . 16

3 HD192639's data analysis **18**
- 3.1 Photometry . . . 18
  - 3.1.1 The TESS Data . . . 18
  - 3.1.2 Light Curves Analysis . . . 19
- 3.2 Spectroscopic Data . . . 26
  - 3.2.1 Corrections to the data . . . 26
  - 3.2.2 Radial velocities . . . 29
  - 3.2.3 Temporal Variance Spectrum . . . 34
  - 3.2.4 Wind spectral lines . . . 37
  - 3.2.5 Rotational velocity . . . 49
- 3.3 Night of the 27-28 July 2021 . . . 50

4 Discussion and conclusion **51**
- 4.1 Discussion . . . 51
- 4.2 Conclusion . . . 54

Chapter 1

Introduction

1.1 Massive stars in the context of modern astrophysics

Despite the fact that they are rare, massive stars ($M_* \geqslant 10\,M_\odot$) of spectral types O or early B are key objects in many processes in the Universe. These objects are hot ($T_{\rm eff} \geqslant 20000$ K) and therefore emit most of their light in the ultraviolet domain. This UV radiation plays a key role in the ionization of the interstellar medium and is at the origin of the nebular emission seen in prominent star-forming regions such as the Orion Nebula or the Carina Nebula.

Owing to the mass-luminosity relation, stars with masses within 10 and 100 $M_\odot$ have bolometric luminosities ranging between several thousands and a million $L_\odot$. Because of these huge luminosities, such objects use up their nuclear fuel within several million years (unlike the Sun, which has an estimated lifetime of 10 billion years). These extremely short lifetimes contribute to the rarity of massive stars. At the end of their evolution, these stars explode in a core-collapse supernova, giving birth to either a neutron star or a black hole. Before this cataclysmic explosion, their evolution proceeds through different steps of nuclear reactions, synthezising heavier and heavier elements in their core, up to the formation of an iron core. The material that has been chemically enriched by these reactions all over the evolution is expelled into the interstellar medium during the supernova explosion, but also, before, via the stellar wind (see below). As a result, massive stars are key players in the chemical enrichment of the interstellar medium.

The enormous luminosities of massive stars have two more important consequences. These stars can be seen from afar, making them the brightest individual objects that can be identified in other galaxies. But even more interestingly, the huge radiation pressure of these stars drives a strong stellar wind with mass loss rates and wind velocities reaching values of order respectively $10^{-6}\,M_\odot\,{\rm yr}^{-1}$ and $1000 - 2000\,{\rm km\,s}^{-1}$. These winds peel off the outer layers of the star, thereby unveiling material that was previously embedded in the stellar core and was chemically enriched by nuclear reactions. In this way, the stellar winds influence the evolution of the stars, enrich the interstellar medium with the ashes of nuclear reactions, and inject copious amounts of kinetic energy into the interstellar medium. Because of this input of kinetic energy, stellar winds probably play a role in the formation of lower-mass stars (either inhibiting the formation of such stars in their neighborhood or triggering the formation of new stars by compressing molecular clouds).

For all those reasons, it is important to better understand the physics of these objects, and especially the properties of their winds. This is the subject of the present work, where we investigate the stellar wind of a massive supergiant star via the observed photometric and spectroscopic variability of the star.

1.2 The variability of massive stars

Spectroscopic variability is an ubiquitous property of O-type stars, especially among O-type supergiants(Fullerton, A. W., Gies, D. R., and Bolton, C. T. 1996). However, there is still considerable debate about the causes of the variability. At the level of the photosphere, this variability could result from non-radial pulsations or rotational modulation of a spotted rotator. Indeed, only a handful of (mainly) late O-type stars have been found to display relatively stable non-radial pulsations with periods of a few hours, similar to β Cep stars. The most prominent examples are ζ Oph and HD 93521. However, the majority of the O-type stars do not show persistent pulsations neither in spectroscopy nor in photometry. On the other hand, the existence of a subsurface convective layer due to an opacity bumpof iron could lead to localized magnetic fields that would manifest themselves as bright spot on the stellar surface (Cantiello, M. and Braithwaite, J. 2011). Owing to the stellar rotation and the time-dependent spot configurations, these spots could produce photometric and spectrometric variability.

Beside the photospheric phenomena such as pulsations and stellar spots, variability of massive stars can also arise in their stellar wind notably for lines such as He II 4686 Å that form partially or completely inside the stellar wind. This can come in two forms which are distinguished according to their scale length. Small scale structures, so-called clumps, result from the intrinsic instability of the radiation pressure driving mechanism of the stellar winds. The clumps take the form of small parcels of material that have higher densities than the ambient wind. Statistical fluctuations of the distribution of these clumps lead to stochastic variations of the emissions that are formed in the wind. Large scale structures can be formed either as the result of the action of a magnetic field on the outflow or from the modification of wind as a result of a locally modified photospheric radiation field (spot). The first scenario applies to stars that have strong dipolar magnetic fields. This situation leads to magnetic confinement of the wind in the plane of the magnetic equator which corotates with the star out to a distance equal to the Alfvèn radius(ud-Doula, A. et al. 2023). Examples of such stars are θ Ori C and HD 191612. In the second scenario the spots, which can be the result of a localized magnetic field, modify the local driving of the wind, leading to overdense regions that rotate with the star in a spiral-like structure that is called a co-rotating interaction region (CIR, Cranmer, S. R. and Owocki, S. P. 1996). An example of what the gas density could be in such region can be found in Fig. 1.

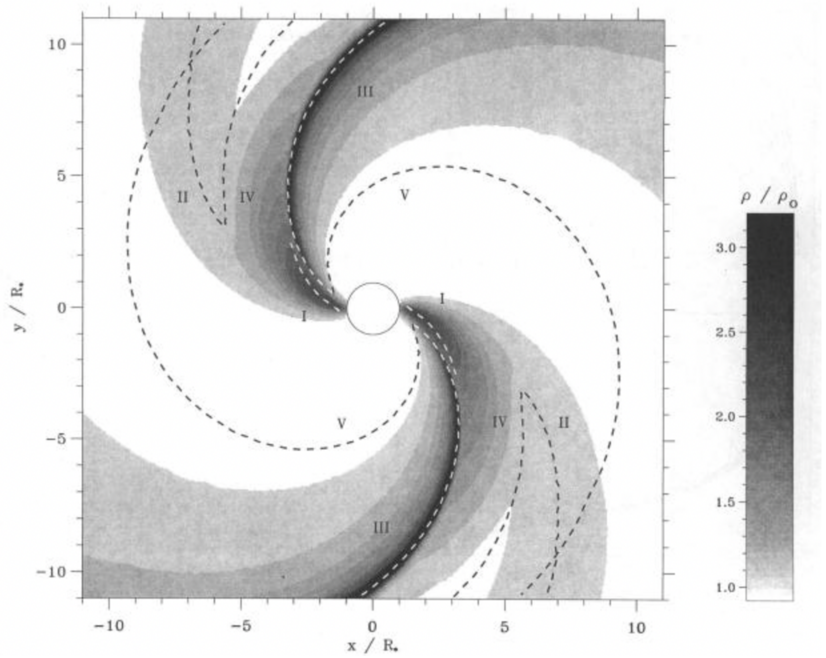

Fig. 1. Normalized density gray scale for a co-rotating interaction region model. Figure taken from Cranmer, S. R. and Owocki, S. P. (1996).

Fullerton, A. W., Gies, D. R., and Bolton, C. T. (1996) suggested a potential link between the observed variability in the star's spectral lines and the variability caused by wind dynamics. They supposed a connection with the photosphere, although they emphasized that while this could be a plausible explanation, it may not be essential to link the two phenomena. At the time, the theory concerning photospheric connections was less developed, leading to some uncertainty in their conclusions. In addition, they offered alternative explanations for wind-induced variability, such as the presence of a weak magnetic field, which could theoretically drive these variations. However, they did not offer a conclusive answer and stellar pulsations could still be a contributing factor.

1.3 Classification of HD 192639

HD 192639 is classified as an O7.5 Iabf-type star (Marcolino, W. L. F. et al. 2022; Shull, J. M. and Danforth, C. W. 2019). This designation indicates that HD 192639 is a massive blue supergiant. O-type stars are the hottest and most luminous stars, with temperatures and luminosities surpassing other stellar types. The "7.5" indicates that this star falls on the cooler end of the O-type category. The "Iab" suffix designates an intermediate supergiant, and the "f" represents the presence of nitrogen (N III 4634-41) and helium (He II 4686) emission lines, a common feature in such stars. Previous studies have focused extensively on the variability of these helium lines, providing insight into the star's emission and absorption behavior (Rauw, G. and Vreux, J.-M. 1998; Rauw, G., Morrison, N. D., et al. 2001).

1.4 Observational History and Previous Results

From Rauw, G. and Vreux, J.-M. (1998), we learn that the earliest reports about line variability for this star date back to the work of from Mannino, G. and Humblet, J. (1955). Other authors reported changes of various lines like the He I λ 10830 emission line (Andrillat and Vreux, 1979), the Hα and He II λ 4868 emission lines (Underhill, 1995a), the C IV $\lambda\lambda$ 5801,5812 absorption lines, and the He I λ 5876 P-Cygni profile(Fullerton, A. W., Gies, D. R., and Bolton, C. T. 1996). While He I λ 10830 was not further investigated due to technical issues (the IR detector was not replaced/detector termination), three runs of observations were made in 1995, 1996, and 1997 at the Observatoire de Haute Provence (OHP)(Rauw, G. and Vreux, J.-M. 1998). Following that, two more runs were made in 1998 and 1999 also from the OHP (Rauw, G., Morrison, N. D., et al. 2001).

The first observing campaign in 1995 confirmed a non-typical profile morphology for He II λ 4686. The observations covered between λ 4530 and 4720 Ångströms, with a spectral resolution of 1.0 Å. The next two runs (1996-1997) focused on the wavelength range between 4100 and 4950 Å with a spectral resolution of 1.2 Å. In 1998, 25 blue (4460-4880), and 18 red (6360-6740) spectra were taken with a spectral resolution of 0.6 Å. In addition, data from the Ritter observatory was used to fill the day gap. While covering a smaller spectral range, these data had a better spectral resolution. In 1999, the spectra were taken between 4100 and 4950 Å with the same spectral resolution as in 1996-1997, 1.2 Å. The main results in Rauw, G. and Vreux, J.-M. (1998) are about the He II 4868 P-Cygni profile presenting variations in intensity, shape and equivalent width. Rauw, G., Morrison, N. D., et al. (2001) also used the data acquired by that previous study.

To quantify this variability, the research from 1998 used the first order moment of the line. This quantity is defined as $W_n = (\frac{c}{\lambda_0 v_\infty})^{n+1} \int_{line} (\frac{F_\lambda}{F_c} - 1)(\lambda - \lambda_0)^n d\lambda$ with $n = 1$. This moment showed a systematic trend towards negative values during the blueward incursion of the emission peak. Radial velocities show variations over a range of about 200 km/s for the dominant peak of the emission.

Other lines were also considered and studied. N III $\lambda\lambda$ 4634-4641 showed no variation of the radial velocity, but a weak intensity variation, only weakly correlated to He II λ 4686. This tends to show that the N III lines are mainly produced in the photosphere, whereas He II 4686 would mostly arise inside the stellar wind. Hβ, Hγ, CIII 4647-50, and He I 4471 showed variability strongly correlated to He II λ 4686. The line profile variability showed a tentative period of about 5 days. However, because the duration of the observing run was not much longer than the proposed period, the uncertainty on this periodicity remained significant.

Using the entire data set, the research from 2001 computed the Temporal Variance Spectrum to identify the lines with the most prominent variations. The following lines were observed with a significant variability: He II λ 4200, Hβ, He I λ 4471, C III $\lambda\lambda$ 4647-50, and the Hβ absorption lines, the He II λ 4686 P-Cygni, and N III $\lambda\lambda$ 4634-41 emission lines, as well as in the red band the He I λ 6678 absorption line and the $H\alpha$ P-Cygni profile. For other lines, a very low level of variability was confirmed: He II $\lambda\lambda$ 4542, 6406, 6527, and λ 6683 absorption lines; Si IV $\lambda\lambda$ 6668, 6701 showed no variation. The He II λ 4686 and Hβ lines showed variations similar to those observed in 1998, although there was not a perfect correspondence.

The research of the period used the Ritter data, processed with an average filter to improve the S/N ratio. They used a generalized spectrogram Fourier method analysis with a uniform wavelength step of 0.2 Å to get a 2-D power spectrum. Finally, they calculated a period of 4.76 days with an uncertainty of a tenth of a day. Int the red data, two secondary frequencies appeared but remained uncertain. The second was very close to the lowest limit frequency that can be sampled and the third could be due to a harmonic. At every wavelength step, the time series were fitted using the following expression:

$$\begin{aligned} F(v,t) &= c_0(v) + a_1(v)\sin\left(2\pi\nu_1[t-t_0]\right) + b_1(v)\cos\left(2\pi\nu_1[t-t_0]\right) \\ &= c_0(v) + \mathrm{Ampl}\,\sin\left(2\pi\nu_1(t-t_0)+\phi_0\right) \end{aligned} \tag{1.1}$$

In this equation, ν_1 stands for the frequency associated with the 4.76-day period, t_0 is an arbitrary reference time, $Ampl$ is the amplitude of the variations, and ϕ_0 stands for the phase constant.

The analysis gives pieces of information about different parameters. The ϕ_0 parameter remains constant as a function of wavelength in the absorption and varies strongly over the emission. There is a local minimum in the amplitude at a velocity of about -40 km/s. The intensity of the emission varies with the strength of the absorption. The phase constant decreases a bit to negative velocities for the Hα line (Rauw, G., Morrison, N. D., et al. 2001).

1.5 Possible Origins of Stellar Wind Variability

The radial velocity of this star varies over a small range, typically with a semi-amplitude of 5 km s^{-1} for He II 4542. From this, the research from 1998 proposed that binarity was an unlikely explanation for the observed variability. In most absorption lines, a part of the RV variations is simply due to the line profile variability. While the possibility of a binary cannot be completely excluded, and probably won't ever be. A changing stellar wind emission seems a more likely scenario to account for the telescopic variability (Rauw, G. and Vreux, J.-M. 1998).

Other explanations can be considered: photospheric variability, corotating interacting regions, and a strong magnetic field confining the wind toward the magnetic equator. The latter two explanations are based on the premise that the phenomenon is coming from a perturbation in the stellar wind. As the He II line considered here would be strongly impacted by such perturbations, this supposition seems plausible. The observed variability would then come from a nonspherical symmetry in the wind and a large-scale structure in the low-velocity part of the wind. Small-scale inhomogeneities seem not plausible at that point, as they should lead to stochastic variations, whereas the observed variability of HD 192639 could be stable over several years.

The period of 4.8 days, persistent over at least four years, could be due to the wind, which would rotate in one block close to the star (within the Alfvèn radius) due to a strong magnetic field before reversing to trajectories determined by the radiative pressure. A confined corotating wind is due to a large-scale magnetic field, but such fields are usually oblique hence leading to a variable aspect angle of the confined wind as a function of rotational phase. A structure due to a bright spot would offer an alternative which seems in accordance with the model of Harries (2000) but has some discrepancies. The variations observed in He II 4686 line were similar but the line profile variations occured at much smaller velocity range than predicted by Harries (2000). Moreover, the Hα line behaviour was different from the predictions of the model. Those models give plausible explanations but are still too simple to perfectly fit the data (Rauw, G., Morrison, N. D., et al. 2001).

Petit, V. et al. (2019) analyzed data to find whether or not some O-type stars, among which HD 192639, have a strong magnetic field. Their study failed to detect a strong (kG) dipolar field for the star studied here. Either HD 192639 does not have a magnetic field, or it could be too close to the detection threshold to be easily identified. These authors also derived, using the Bonnsai model, information about the star and its evolutionary stage. While the exact results are heavily dependent on the model used, they are good enough to estimate roughly where the star stands on its evolutionary scale. They estimate that HD 192639 is about 3 million years old for 38 $M_\odot$. For that mass and that age, it should be at three quarter of its main sequence.

This star is situated at about 2.13 kpc (Shull, J. M. and Danforth, C. W. 2019). This is found through the use of the Gaia DR-2 parallax. Hawcroft, C. et al. (2021) studied the characteristics and wind parameters of multiple O-type stars using the FastWind code and Marcolino, W. L. F. et al. (2022) repeated a similar study using CMFGen models. Both give a good idea of the stellar and stellar wind parameters. Table 1.1 summarizes the fundamental stellar parameters as determined by their respective methodologies.

Table 1.1: Stellar and wind parameters determined by Hawcroft and Marcolino

Parameter	Hawcroft (FastWind)	Marcolino (CMFGen)
T_{eff} (kK)	33.5 ± 0.5	33.5
R_{eff} (R$\odot$)	20.7 ± 0.6	20.72
v_∞ (km s^{-1})	2700 ± 100	1900
$log \dot{M}$ ($M_\odot$ yr_{-1})	-5.85 ± 0.05	-5.27
v sin(i) (km s^{-1})	103 ± 14	N/A

The two methods give similar result except for the terminal velocity. However, Hawcroft himself present that value as dubious. Unfortunately, v sin(i) was only available in Hawcroft, C. et al. (2021).

Markova, N. et al. (2005) proposed different models to explain line profile variabilities after studying multiple O-type stars, among which HD 192639. While a model assuming a homogeneous wind with a spherical symmetry was found to be sufficient to reproduce the overall properties (morphology and strength) of the mean Hα line profile, such a model does not explain the line's variability, which they rather attributed to fluctuations of small-scale inhomogeneities. For their analyses, they used multiple observations, spread over days weeks and months. However, in the specific case of HD192639, the sampling was clearly not dense enough to investigate variations on the 4.8 days timescale previously reported by Rauw, G., Morrison, N. D., et al. (2001).

The stars in their sample had previous evidence of variability in the UV and optical range and indirect evidence for the presence of clumps in the wind. Markova, N. et al. (2005) specifically looked for variations in the Hα line. Analysing their data with a modified Temporal Variance Spectrum (TVS) method; they found Hα variability for multiple stars. They attributed this to the combined effect of the photosphere and the stellar wind.

The two models they propose, shell/ broken shell and the large-scale co-rotating wind structure, both have their pros and cons. In the end, even those models remain too simple to accurately predict the variability of the stars. They find that over a long time, Hα seems constant but that could be due to their sampling.

1.6 Purpose of this work

In this work, we will analyze photometric and spectrometric data about HD 192639 in order to confirm or refute the previous period propose by Rauw, G. and Vreux, J.-M. (1998) and Rauw, G., Morrison, N. D., et al. (2001). Nothing indicates that the period they discovered is stable over time or that the phenomenon behind it is not transient. Moreover, while the sampling used by Markova, N. et al. (2005) did not allow to easily detect this period, the fact that they did not, can cast a small shadow of doubt about the existence and/or stability of the phenomenon.

Reanalyzing the star, especially with better data, could also lead to the discovery of new phenomena, transient or not. This would be particularly interesting as it could improve our understanding of this star and of massive supergiants in general.

Finally, this work gives a broader perspective of the star as the spectroscopic observations are supplemented by photometric time series. Such high-precision space-borne photometry was not available in the previous studies, but its analyzes could give a more complete understanding of the dynamics of the stellar wind.

1.7 Brief overview of this work

This study will first begin to introduce the different instrument that collected the data used here. This is important to understand the reasons behind the corrections and the way the analysis was done.

Secondly, it will address the data analysis itself. First, with the photometric dataset and then with the spectrometric dataset. More precisely, it will first present the TESS data and the light curves analysis results. Then the motivation and methodology behind the corrections to the spectroscopic data will be explained. The next parts will present the various results from the spectroscopic data. These include the radial velocities, Temporal Variance Spectrum, the Wind spectral lines and the rotational velocity.

Thirdly, we will discuss the meaning of all the results, the underlying principles and what this tells us about HD 192639. We will see that some theories match our results better than others. While none can be completely and formally excluded, some have a very low probability of being responsible of the behavior of this star.

This work will be concluded by a small summary of the refreshed understanding of HD 192639. This will include how our results have modified our view of this star compared with the previous articles. Finally, we conclude this thesis with a brief outline of what remains to be explored and what our study brings to the understanding of massive stars in general.

Chapter 2

Instruments

2.1 TESS

2.1.1 The TESS Mission Design

The Transiting Exoplanet Survey Satellite (TESS) (Fig.1) is a satellite primarily designed to discover exoplanet transits but whose data are used in multiple other fields, such as the survey of variable stars and the observation of transient phenomena. Launched on April 18, 2018, it has the advantage of observing almost the entire sky over time. Indeed, while the observed zone in one month is already large, the planned rotation of the satellite allows the observation of a whole hemisphere in about a year. TESS NASA Website Last accessed 14 november 2024

TESS is on an elliptical high-Earth orbit that provides an unobstructed view of its field to obtain continuous light curves. This orbit is stable and requires no propulsion for station-keeping. Its period is 13.7 days, and TESS changes its Field Of View (FOV) every two periods. This time span, a bit less than a month, is called a sector. It is usually by that name that the associated data set is designated.

The mission design is so that the sky is divided into 26 sectors (Fig.2), 13 north, and 13 south. Each sector encompasses the corresponding north or south ecliptic pole. This allows for an almost constant observation of each pole over about a year.

TESS's primary mission lasted for two years, from July 25, 2018, to July 4, 2020, and after completion, NASA approved a first extended mission, until September 2022 then a second, which should last until 2025.

The first extension comprised cycles 3 and 4. In the 3rd cycle, the southern hemisphere was observed. In the 4th cycle, 16 sectors were used instead of 13 and the ecliptic plane which had been up to then avoided was finally observed.

The second extension continued in that direction, with more ecliptic observations, although it came back to 13 sectors per cycle. This extension consists of 3 cycles, including cycle 7 which is still ongoing.

Fig. 1. Artist view of TESS. Figure taken from TESS NASA Website Last accessed 14 november 2024.

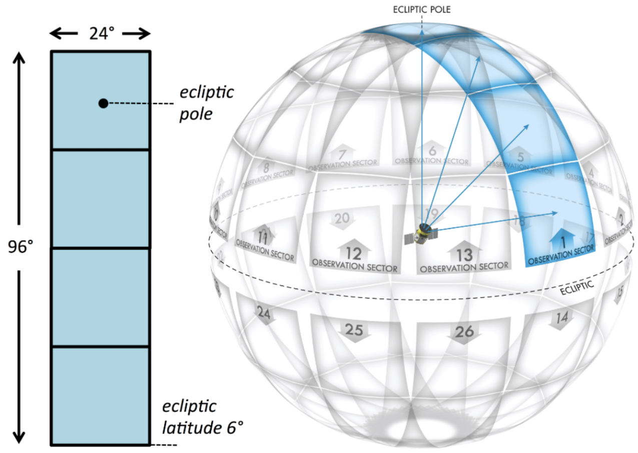

Fig. 2. Artist representation of the different observation sectors of the TESS satellite. Figure taken from TESS NASA Website Last accessed 14 november 2024.

2.1.2 Scientific Instruments and Technical Specificities

TESS carries four wide-field cameras with a combined field-of-view (FOV) of 24x96 square degrees. This FOV is particularly large compared with other telescope set-ups, even that of Kepler only had a 115 square degree FOV (TESS NASA Website Last accessed 14 november 2024).

Each camera possesses a focal plane CCD array as its detector. This array is made of four CCID-80 devices developed by the MIT and the Lincoln Institute. Each CCD is made of a 2048 x 2048 imaging array with pixels of 15x15 microns. Each pixel corresponds to about 21 arcseconds on the sky.

The cameras are also equipped with a long-pass filter to create a cutoff at 600 nm, creating an effective bandpass between 600 and 1000 nm. This bandpass is broad compared to classical filters such as Johnson U, B, V, R, I. Basically, the TESS band covers the R, I, and z filters with its center close to that of the I filter (it is thus like an extended I filter, see the TESS bandpass response function, TESS NASA Website Last accessed 14 november 2024).

The satellite was designed to work as a photometer and not as an imager. Following this idea, it was more important to minimize the noise and to have good photometric stability than to have a compact point spread function (PSF). The result is that the PSF varies significantly across the focal plane. Instead of using this PSF, the TESS satellite uses a pixel response function (PRF), representing the observed appearance of point sources. Given this unusual method, the photometry of an object can be obtained by summing all the pixels in a certain region. This region is called the aperture mask, it can be selected by the pipeline or the user and is, unlike apertures commonly used in photometry, not circular. An example of PRF can be seen in Fig.3.

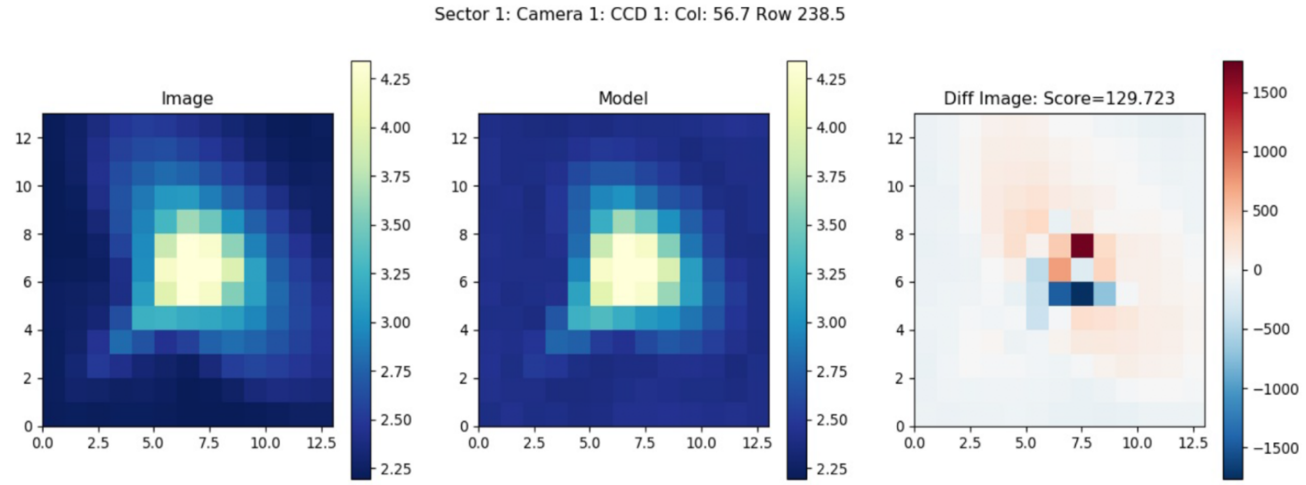

Fig. 3. PRF from sector 1, camera 1. Figure taken from TESS NASA Website Last accessed 14 november 2024.

During the operations, the cameras feed the Data Handling Unit (DHU) a stream of images with an exposure time of 2s. The DHU then processes the CCD images by performing cosmic ray mitigation and collecting pixel sub-arrays. The data is stored and transmitted every 13.5 days before being post-processed on the ground.

The data products are made in two parts: the DHU sums on the fly the 2s images to get (1) individual Full-Frame Images (FFIs) with a given cadence depending on the cycle and (2) sub-arrays data on pre-selected target stars with a cadence of two minutes. The FFIs allow a survey of the full FOV, while the sub-arrays allow a higher cadence monitoring of specific targets chosen in advance. All data are made publicly available after about a month of processing.

The sub-array mode has not changed from cycle 1 to now, but the FFIs' cadence has evolved during the missions. At first, the FFIs were collected every 30 minutes, allowing the observation of fainter targets than those observed in the sub-arrays (cycles 1 and 2). Then, it was decided to reduce that cadence to 10 minutes (cycles 3 and 4) and, finally, to 200 seconds (cycles 5, 6, and now, 7). This progressive acceleration of the cadence was detrimental to the fainter targets but has allowed the study of many additional stars with an increased cadence. The current cadence is close to the cadence of the sub-arrays, thereby focusing more on bright stars than the 1st cycles. Moreover, in the extended missions, a 20-second mode could be requested for chosen targets.

2.1.3 The Data Processing

A first processing is made on board. The DHU can mitigate the impact of the cosmic rays on the data of these FFIs and sub-arrays by removing the highest and lowest values in groups of N pixels. It effectively removes the cosmic rays from the images but increases the shot noise while decreasing the effective exposure time. Simulations showed that the optimal value of N was 10 and it was confirmed during flight that this value is good for both types of data products (TESS Instrument Handbook Version 0.1 (Draft of 6 December 2018) Last accessed 14 november 2024).

The data processing done on the ground depends on the product. The full description and architecture of the science processing operation center can be quite extensive and require multiple steps as can be seen from Fig.4.

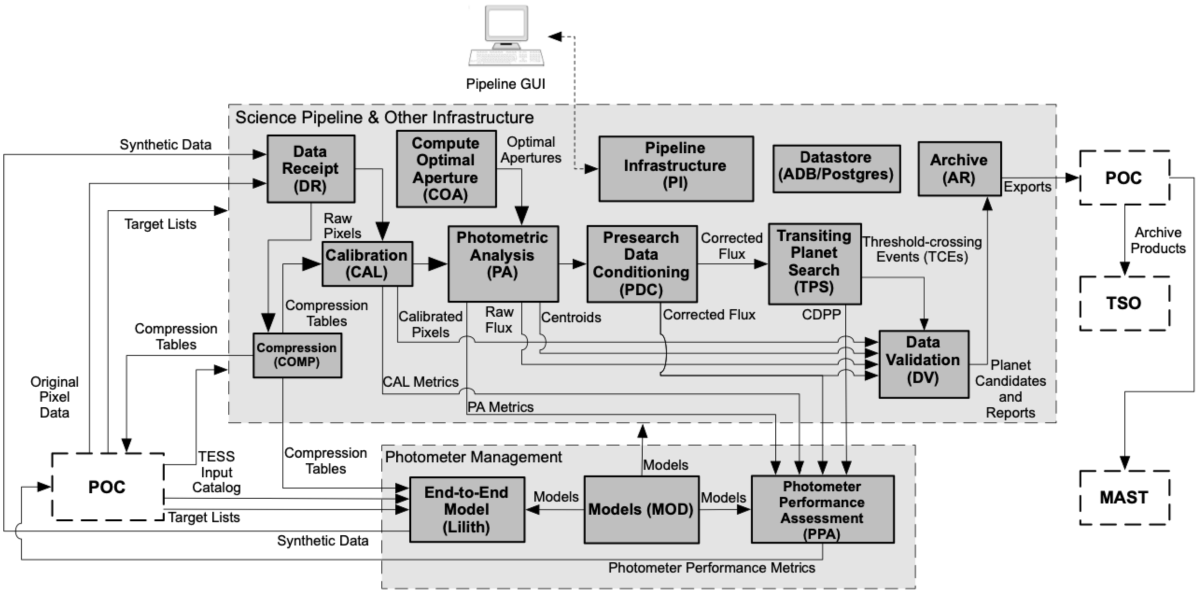

Fig. 4. Architecture diagram of the SPOC with its major components, including the TESS science pipeline. Figure taken from Jenkins, J. M. et al. (2016).

The compression (COMP) module is used to generate compression tables to compress the pixel data during the flight and reduce the storage requirement aboard the satellite. The 2-minutes and FFIs have their own separate compression algorithms.

The calibration (CAL) removes instrument effects and other artifacts from the data. Traditional data reduction is performed, such as bias and dark current and flat field correction. Additionally, pixel calibrations, TESS-specific corrections, and other types of operations are performed. CAL operates on both the 2-minute data and FFIs and produces calibrated pixel flux time series, uncertainties, and other metrics used in other operations.

Compute optimal aperture (COA) identifies the 100 pixels allocated to each preselected target star in the CCD images. The selected pixels will then be used for photometry and astrometry. In this case, there is a notable difference between TESS and Kepler: the last one only used 32 pixels per star. This increase in the number of pixels for TESS relaxes the requirement on predicted pointing accuracy.

The photometry analysis (PA) measures the brightness of each requested target on each 2-minute frame. It also removes zodiacal light and the diffuse stellar background. Finally, it measures the centroid of each star on each frame. It produces the single aperture data (SAP) of each target star.

The presearch data conditioning (PDC) performs an important set of corrections to the light curve produced by PA. It includes the identification and removal of instrumental signatures, of isolated outliers and corrects the flux time series. It produces the PDCSAP data of each target.

There is also a further component to the data processing, but it is aimed at detecting potential exoplanets and is not relevant to our study.

As the FFIs are not further processed by the pipeline, the star counts must be extracted by other means. The selection of the target pixels, the background reduction, and all subsequent processes are made outside of the TESS pipeline using the PYTHON package LIGHTKURVE. This will be more developed in subsection 3.1.1, explaining how the flux data of sector 14 and 15 were processed.

2.1.4 Limitations

Despite its many advantages, TESS has some limitations:

It has a low resolution but a wide field of view. TESS has a pixel size corresponding to 21 arcseconds, almost six times more than the 3.98 arcseconds for Kepler and about 65 times the 0.32 arcseconds squared of HST. The aperture mask is usually large, 1 to 3 pixels. This makes it more difficult to avoid contamination from other sources near the target. Catalogs such as the TESS input catalog (TIC) or GAIA-DR3 provide information to estimate the contamination.

In addition, TESS orbit ensures a wide coverage of the sky, but most parts are only observed for 27 days every two years on average, limiting the study of longer-term variation.

2.2 Tigre

The TIGRE telescope (Fig. 5), situated at La Luz observatory near Guanajuato (altitude 2435 m), has a primary mirror with a diameter of 1.2 m. Currently, its sole instrumentation is the spectrograph HEROS, an Echelle spectrograph with a spectral resolution R about 20 000. Before 2012, it was still installed at Hamburg observatory and could only observe in the blue channel. In April 2012, the red channel was added, shortly before the telescope was shipped to Mexico where it arrived in 2013 and remains until now. Three institutes manage the telescope: the previously mentioned Hamburg observatory, the University of Liège and the University of Guanajuato. Two of the three institutions are thousands of kilometers away from the instruments, this is not an issue as the telescope is operated normally in a completely robotic mode, with only some remote checking, needing no human presence on site, except for periodic (about once per year) maintenance missions.

The blue channel is able to observe between 3740 and 5740 Ångstrom while the red channel covers the range between 5770 and 8830 Ångstrom. Both channels are equipped with Andor iKonL CCD cameras with E2V 2K×2K chips and a pixel size of 13.5 μm.

Obviously as a ground based telescope, the observing time is depending on the weather, humidity and wind. Moreover, due to a poor power plant powering the site, the risk of power outage is non negligible. During the first years in Mexico, the telescope experienced an average of 25 outages per year at night, that number has reduced almost by half now (González-Pérez, J. N. et al. 2022).

Fig. 5. Cupola of the Tigre telescope. Figure taken from González-Pérez, J. N. et al. (2022).

Chapter 3

HD192639's data analysis

3.1 Photometry

3.1.1 The TESS Data

HD192939 has been observed by TESS in sectors 14, 15, 41, 54, 55, 75, 81. Except for the first two sectors, HD192939 was a target star hence fully processed 2 min light curve data are available.

For sectors 14 and 15, only FFIs with a 30 min cadence are available, and the light curves were built using the LIGHTKURVE package.

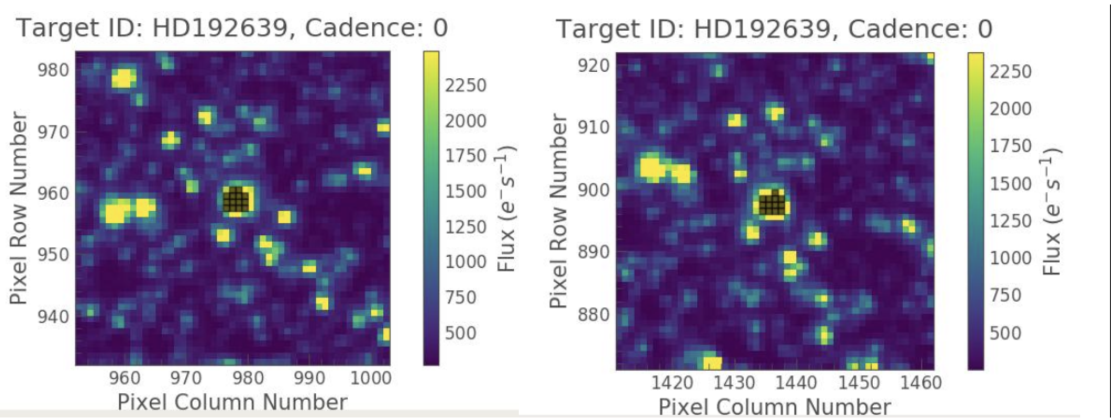

Fig. 1. Pixels selected for the source aperture mask in sector 14 and 15 (left and right respectively)

First, 51x51 cutout images centered on the source were downloaded from TESS archives, and then pixels associated to the source were chosen using a flux cutoff, 30 times the median flux, around the center of the FOV (fig.1). The background pixels are those in the FOV with fluxes below the median. The background correction was performed using two different methods: subtraction of a simple median of the fluxes in the background pixels and subtraction of a background value adapted to the source point using a principal component analysis (pca) with 5 components. Both data sets were treated to exclude the points where the error over the magnitude was larger than the mean error plus 3 times the standard deviation of errors ($\sigma = \sqrt{\frac{\Sigma(E-M_E)^2}{N-1}}$, with E the errors on the magnitude, M_E the mean error and N the number of points). This excludes potentially problematic points. The pca method is more advanced and better at removing trends. Besides, the light curves did not have any obvious issues, so the pca data were selected for our analysis.

As mentioned before, for those sectors with full high-cadence photometry, the pipeline provides two sets of data, the SAP and the PDCSAP light curves. The PDCSAP data has less systematic trends than the SAP and the light curves didn't have obvious issues, so the PDCSAP data were selected for our analysis.

3.1.2 Light Curves Analysis

The next step of the analysis is done by using a Fourier transform to find whether periodic signals are present in the star's light curve. In our case, we use the method of Heck, A., Manfroid, J., and Mersch, G. 1985. Concretely, it allows to partially bypass the problems caused by a nonuniform sampling dataset with holes, as often occurs in astronomy. TESS data do not have many problems in this respect, so the correction is not large, but the spectroscopic data that we analyze in section 3.2 will be more sparse and for homogeneity, we use the same method for both photometric and spectroscopic data.

The TESS data are provided as fluxes. These fluxes were converted into millimagnitudes using the usual formula $mmag = (-2.5log(F) - M) * 1000$ with mmag the millimagnitude associated with the flux F, and M the mean magnitude. The mean magnitude value was subtracted to normalize the data. Fig.2 to Fig.8 show the light curves of the different sectors.

From those light curves, no clear period can be detected just by visual inspection. Some structures can be seen as in Sector 81 after 10520 days, but nothing persistent or truly periodic. There are clearly some small flux variations; the light curves are not flat and constant. To be sure if anything is truly significant, a comparison between the errors on the magnitude with the standard deviation of the magnitude is needed. Table 3.1 shows the different errors and standard deviations for each sector.

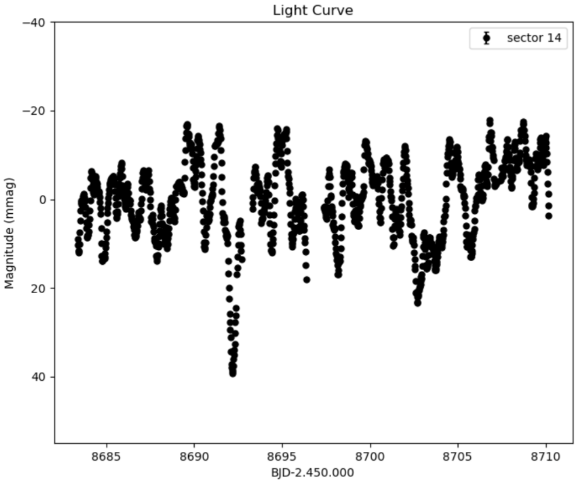

Fig. 2. Light curve of HD192639 during Sector 14.

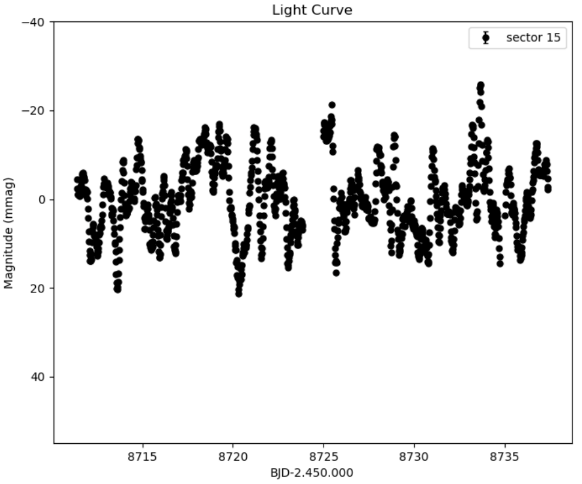

Fig. 3. Light curve of HD192639 during Sector 15.

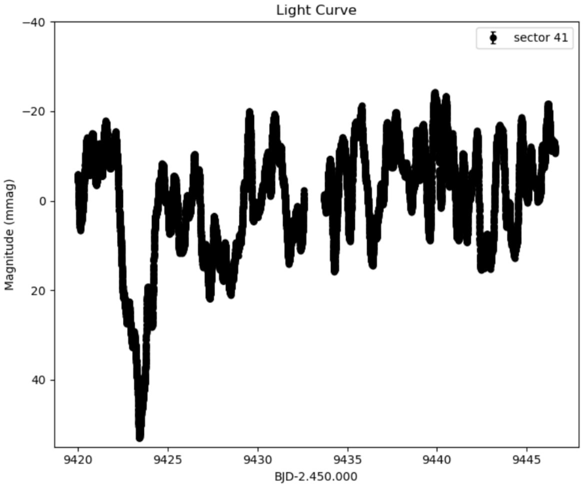

Fig. 4. Light curve of HD192639 during Sector 41.

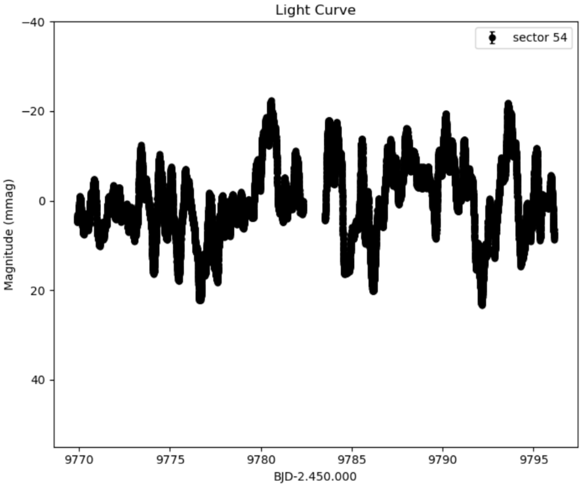

Fig. 5. Light curve of HD192639 during Sector 54.

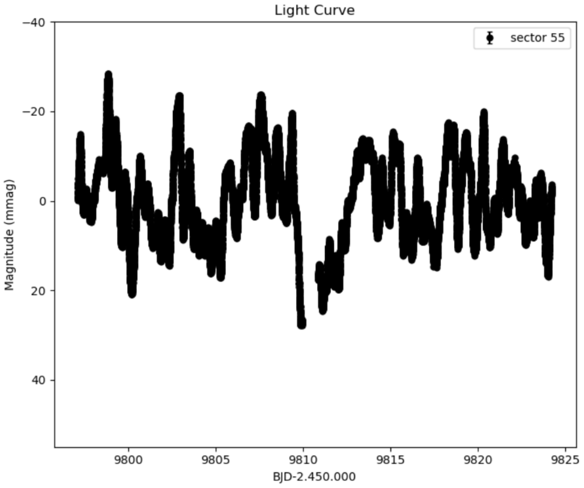

Fig. 6. Light curve of HD192639 during Sector 55.

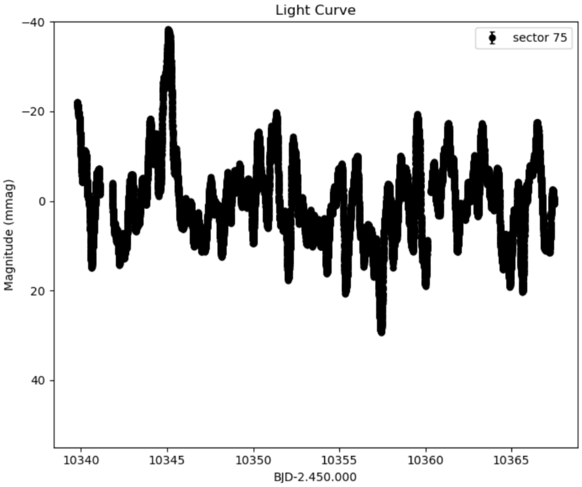

Fig. 7. Light curve of HD192639 during Sector 75.

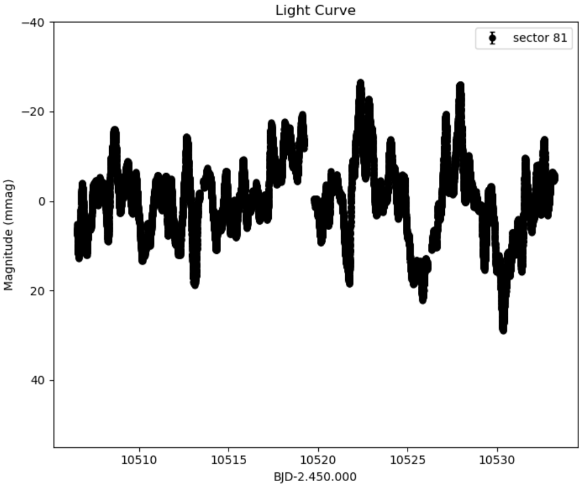

Fig. 8. Light curve of HD192639 during Sector 81.

Table 3.1: Comparison between the mean errors and the standard deviation of the magnitudes

Sector	mean error (mmag)	standard deviation (mmag)
14	$5.479 * 10^{-2}$	9.276
15	$5.573 * 10^{-2}$	8.158
41	$2.153 * 10^{-1}$	10.382
54	$2.163 * 10^{-1}$	8.621
55	$2.158 * 10^{-1}$	9.811
75	$2.188 * 10^{-1}$	9.618
81	$2.137 * 10^{-1}$	8.985
Combined	$2.119 * 10^{-1}$	9.244

The errors are much smaller than the standard deviation in all circumstances by at least a factor 10. This means that all the variations in the light collected are due to variations of the star itself and not some measurement issue. The mean errors come from the TESS files and have been transformed from errors on the flux to errors on the magnitude, then the arithmetic mean was computed to get the values in table 3.1. The standard deviation on the magnitude has been calculated using $\sigma = \sqrt{\frac{\Sigma(Mag-M_{Mag})^2}{N-1}}$.

In Sector 41, only the part after BJD 2459425 was considered, given that the dip at the beginning of this Sector feature is clearly exceptional and not from the "usual regime" of the star. If it was considered in the estimation of the standard deviation error, sector 41 deviation would be 13.09 mmag and the standard deviation of the whole dataset, 10.11. To better characterize the timescales and regularities of the variations, we then computed the Fourier spectra of the TESS time series using the method of Heck, A., Manfroid, J., and Mersch, G. (1985).

The frequency spectra in linear scale are shown from Fig.9 to Fig.15, and in log-log scale on Fig.16 to Fig.22. A structure typical of red and white noise can be observed. In the log-scale figures, this is best seen as a first plateau before 10^0 day^{-1}, a slope and then another plateau, roughly after 10^1 day^{-1}. The "linear" periodogram and the logarithmic scale ones are not displayed over the same frequency range as the log-scale plots were optimized to illustrate the red-noise and the transition to the white noise. The focus in the linear scale periodograms is on the lower frequency domain, where most of the stellar variability taked place. The FFIs data allowed for a search between 0.04 day^{-1} and about 24 day^{-1}. As the 2-minute data allowed the search of higher frequencies the search went up to 360 day^{-1}. The frequency spectra were calculated with frequency steps of 0.003 day^{-1} corresponding to a dataset of 28 days duration (which is about the duration of 1 sector). The Fourier spectra were computed up to the Nyquist frequency (24 day^{-1} and 360 day^{-1} for sectors 14, 15 and sectors 41, 54, 55, 75, 81, respectively, because of their cadence). No signal appears at frequencies above 4 day^{-1} and the highest peaks are located at frequencies below 1 day^{-1}. At this stage, it is important to emphasize that the red noise, that is the increase of the amplitude of variations towards low frequencies, is not an instrumental feature but arise from genuine variations of the light emitted by the star. The existence of a red noise component in the Fourier spectra of the photometric data is indeed a very common property of massive stars(Nazé, Y., Rauw, G., and Gosset, E. 2021).

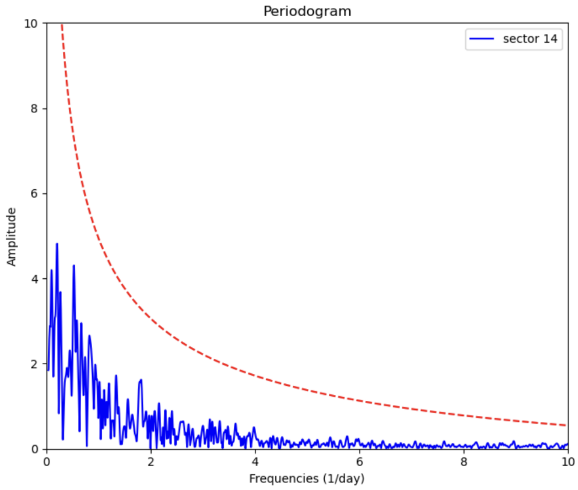

Fig. 9. Periodogram of the light curve of HD192639 during Sector 14. In red, the limit of significance of the peaks.

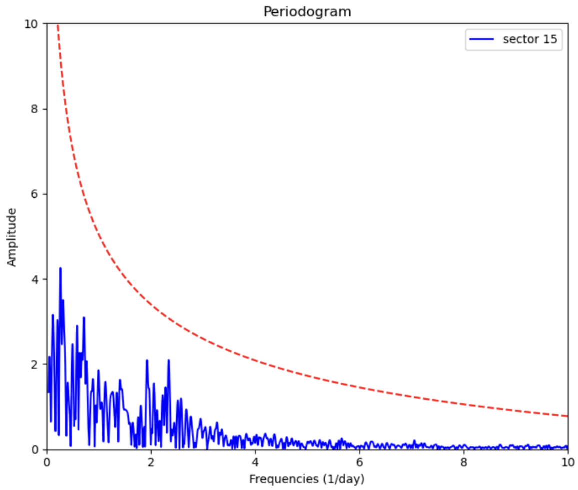

Fig. 10. Periodogram of the light curve of HD192639 during Sector 15. In red, the limit of significance of the peaks.

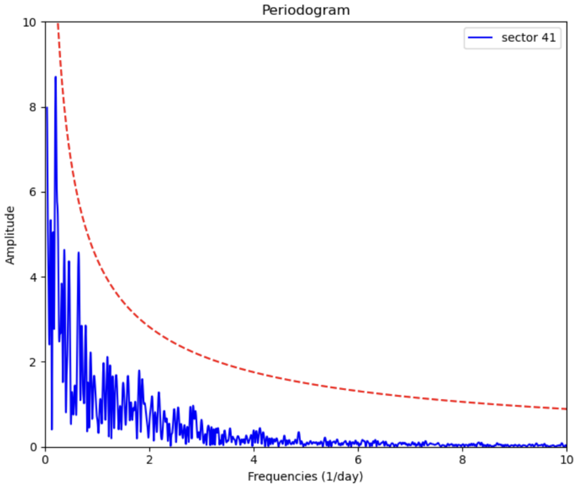

Fig. 11. Periodogram of the light curve of HD192639 during Sector 41. In red, the limit of significance of the peaks.

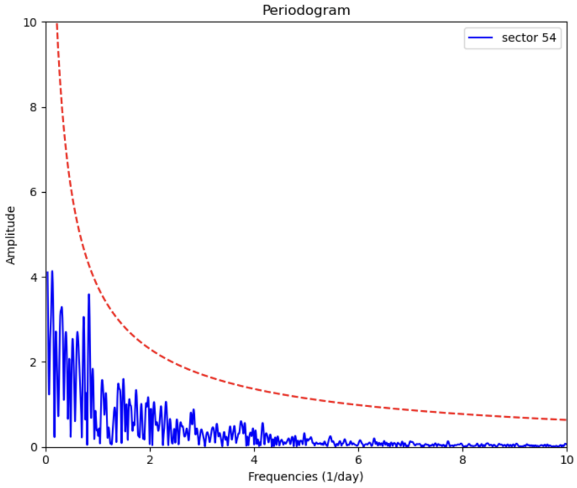

Fig. 12. Periodogram of the light curve of HD192639 during Sector 54. In red, the limit of significance of the peaks.

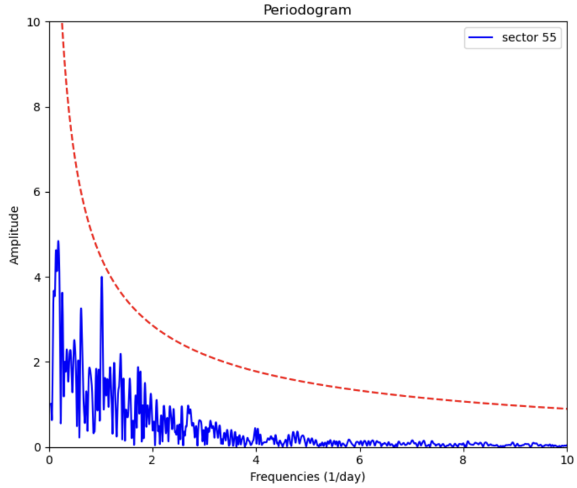

Fig. 13. Periodogram of the light curve of HD192639 during Sector 55. In red, the limit of significance of the peaks.

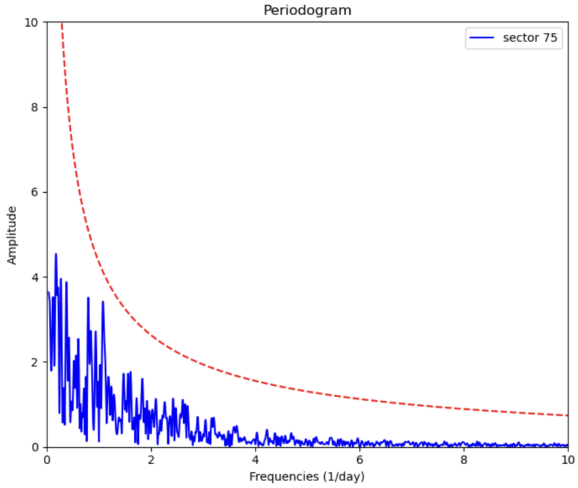

Fig. 14. Periodogram of the light curve of HD192639 during Sector 75. In red, the limit of significance of the peaks.

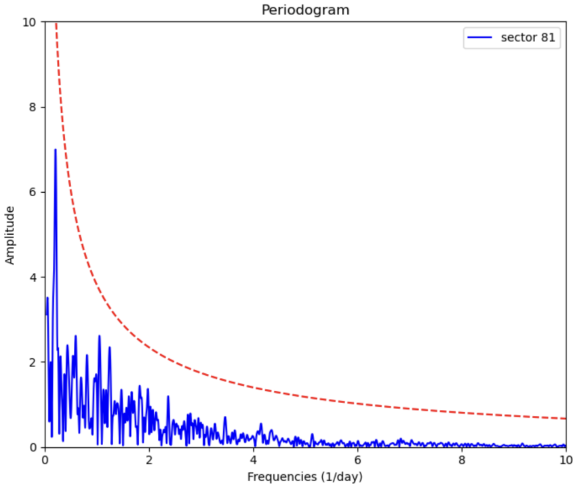

Fig. 15. Periodogram of the light curve of HD192639 during Sector 81. In red, the limit of significance of the peaks.

The global shape of the periodograms can be modeled using the following description:

$$A(\nu) = C + \frac{A_0}{1 + (2\pi\tau\nu)^\gamma} \tag{3.1}$$

As used in Nazé, Y., Rauw, G., and Gosset, E. (2021), this equation combines white and red noise: C is the white noise level, A_0 the red noise level at null frequency, τ the mean lifetime of the structures producing the red noise, and γ the linear slope decrease. This expression was adjusted to the logarithmic scale periodogram. Starting from some initial guesses for the model parameters, we optimized these parameters using a Levenberg-Marquard method (Gavin 2013). The best-fit model parameters obtained in this way are given in table 3.2.

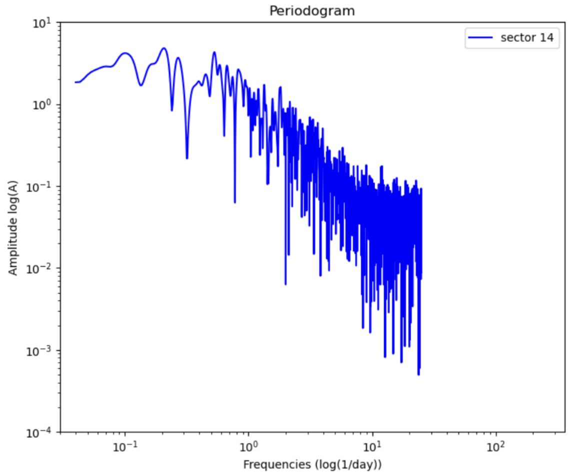

Fig. 16. Periodogram of the light curve of HD192639 during Sector 14 in logarithmic scale.

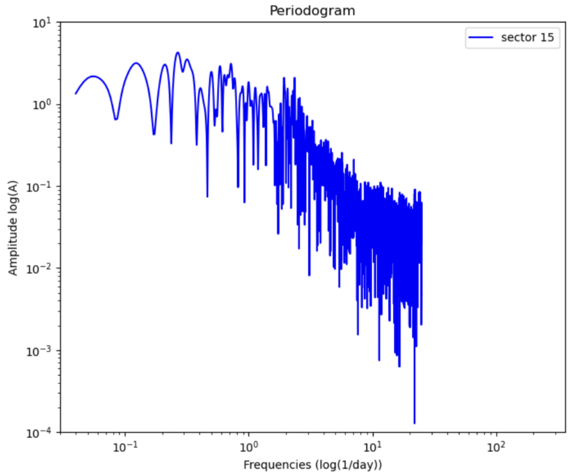

Fig. 17. Periodogram of the light curve of HD192639 during Sector 15 in logarithmic scale.

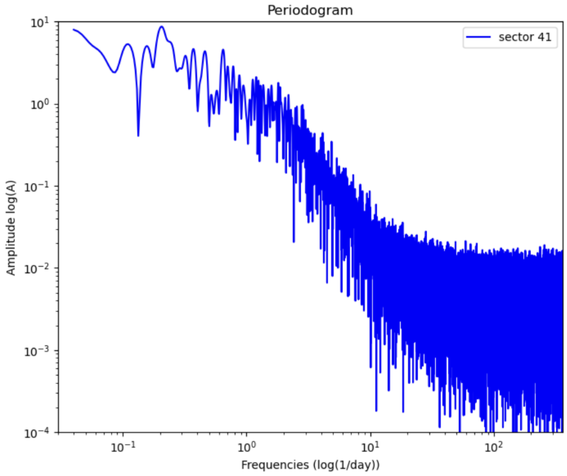

Fig. 18. Periodogram of the light curve of HD192639 during Sector 41 in logarithmic scale.

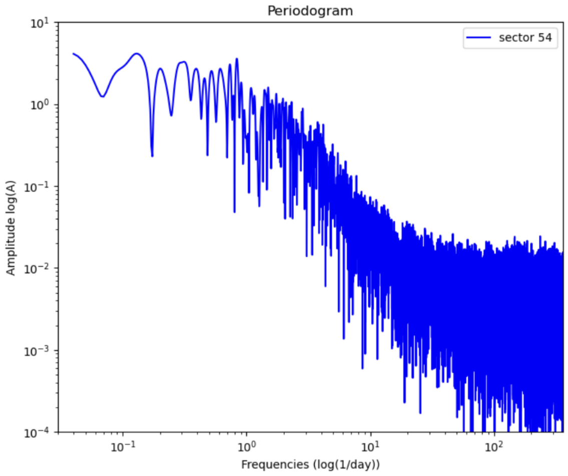

Fig. 19. Periodogram of the light curve of HD192639 during Sector 54 in logarithmic scale.

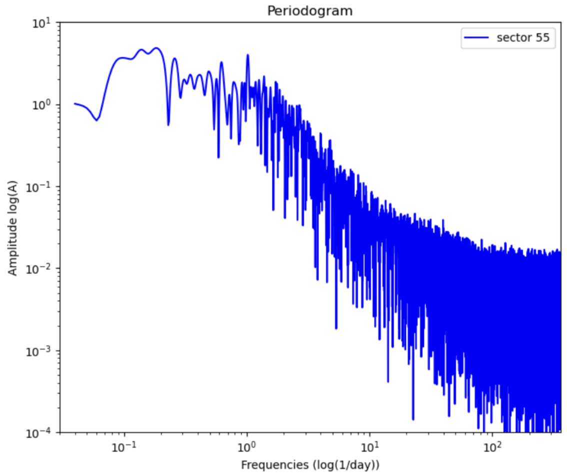

Fig. 20. Periodogram of the light curve of HD192639 during Sector 55 in logarithmic scale.

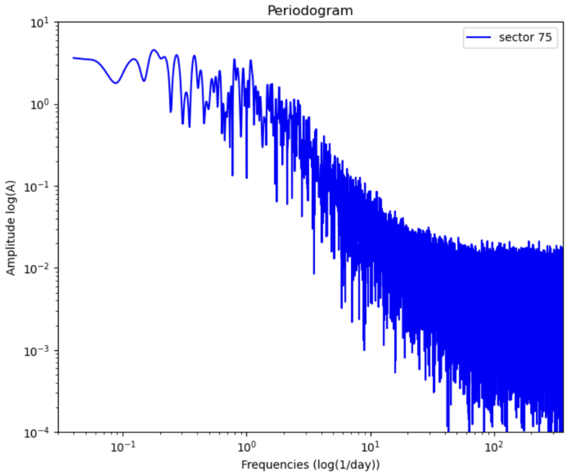

Fig. 21. Periodogram of the light curve of HD192639 during Sector 75 in logarithmic scale.

Using these best-fit parameters, we obtain a good representation of the red+ white noise level: any significant signal will be well above it. We choose a threshold of 5 times this level so that there is 0.00006% chances that the period is due to a fluctuation in the noise. This can be seen in Figs. 9 to 15 as the red dashed line. As it can be observed in those figures, no peak crosses this threshold. Under those circumstances, no significant frequency is detected in the photometric data.

It is however interesting that several sectors display their strongest peak in the Fourier periodogram close to a frequency of 0.21 day^{-1}. This is the case for sector 14, 15, 41 and 81. While these peaks are only at 2-3 times above the fitted red noise level, the fact that they are always found near the same frequency suggests that this timescale has a real astrophysical meaning.

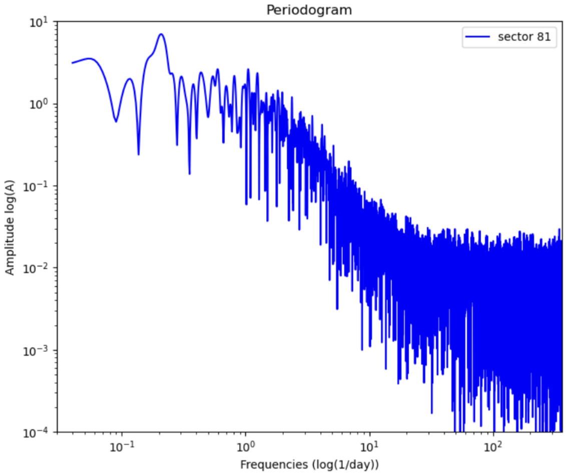

Fig. 22. Periodogram of the light curve of HD192639 during Sector 81 in logarithmic scale.

Table 3.2: Red and white noise model parameters

Sector	C (mmag)	A_0 (mmag)	τ (day)	γ
14	-0.23	10.27	4.71	0.59
15	-0.41	7.75	4.31	0.45
41	-0.03	9.93	4.96	0.66
54	-0.03	9.67	4.63	0.71
55	-0.03	9.97	4.86	0.66
75	-0.02	11.72	4.49	0.74
81	-0.02	9.67	4.64	0.71

3.2 Spectroscopic Data

Spectroscopic data of a star give information mainly about three topics. The temperature of the said star, its chemical composition and its radial velocities. In the case of HD192639, the temperature as well as the CNO abundances have already been determined (Martins, F. et al. 2015) and will not be explored further here. We will examine the radial velocity of this star.

The spectroscopic data used here can be separated in two parts, the 108 blue spectra and the 108 red ones. The blue spectra cover 3737 to 5748 Å. From the red spectra two regions of interest were selected for this study, focusing on the absorption P-Cyg profile of He I 5875 and the P-Cyg profile of Hα 6563. Those two regions are respectively 5860-5919 Å, and 6450-6789 Å. We note that the remainder of the red spectrum is either heavily contaminated by strong telluric absorptions or contains no stellar lines. In both cases, red and blue, the wavelength step between two points is 0.09 Å.

3.2.1 Corrections to the data

With spectroscopic data taken from the ground, an important thing to do is to correct for telluric absorption in the wavelength domain considered. The blue channel is not affected by such absorptions, but the red channel is heavily affected by the absorption of atmospheric water vapors. To have a reading as accurate as possible of the spectrum of HD192639 in the red channel, it is necessary to correct those absorption lines before undertaking any quantitative analysis. What is especially crucial in this context is the fact that the strength of those telluric absorptions varies from night to night.

To do so, a template spectrum representing the atmospheric absorption is selected (Hinkle, K. et al. 2000). For each observed spectrum, this template is shifted in wavelength and scaled in intensity to match prominent telluric lines in the observed spectrum. The shifted and scaled template is then applied to the observation to correct it for the telluric absorptions. The strength of the telluric lines depends on the airmass at the time of the observation as well as on the weather (humidity). To correct the observed spectra, the shift and the scaling factor of the template are first determined manually before a small optimization is performed. Both processes were done with the Iraf program developed by the National Optical Astronomy Observatory (NOAO) in U.S.A.

After this correction over the red channel spectrum, both the blue and red channels needed to be normalized to the continuum to work with the same relative intensities of the spectral lines for all data and remain coherent throughout the analysis. This step is especially crucial to avoid introducing any artificial spectroscopic variability related to a changing shape of the continuum. To do so, the MIDAS program developed by ESO was used to fit a polynomial approximation of the continuum over each of the spectra separately. To perform this normalization, 53 points of the continuum were taken in the blue channel, 20 in the He I region of interest, and 47 in the Hα domain.

After telluric correction and normalization, the 324 spectra are ready to be analyzed, but it is important to know what the most important spectral features are present in these data. In order to pinpoint the different lines, a mean spectrum of each region was created for the identification of the lines. In Figs. 23 to 32, the different ranges are shown with the different lines identified.

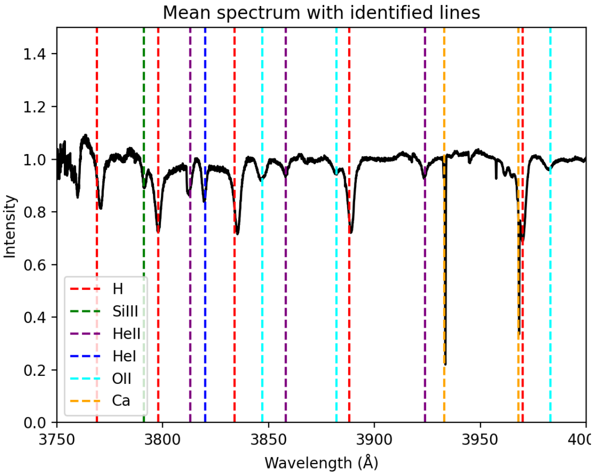

Fig. 23. 3750 to 4000 Å.

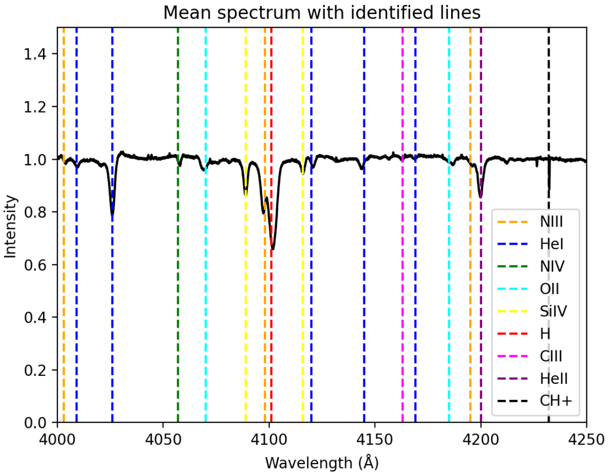

Fig. 24. 4000 to 4250 Å.

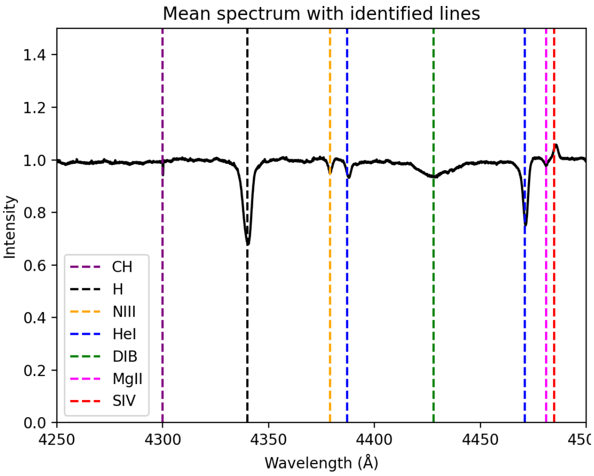

Fig. 25. 4250 to 4500 Å.

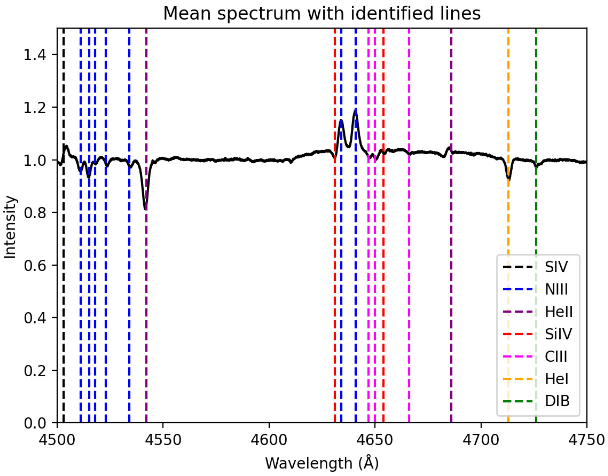

Fig. 26. 4500 to 4750 Å.

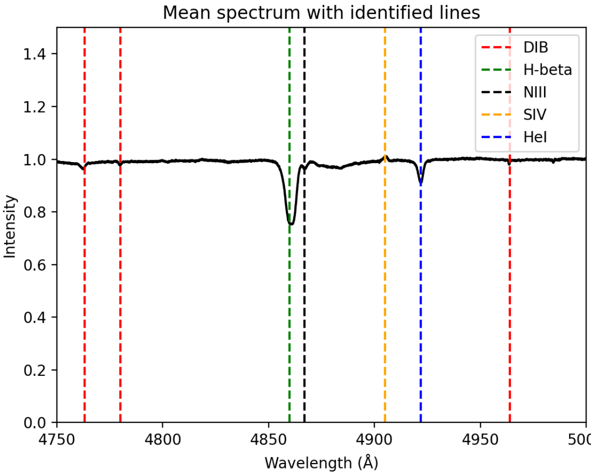

Fig. 27. 4750 to 5000 Å.

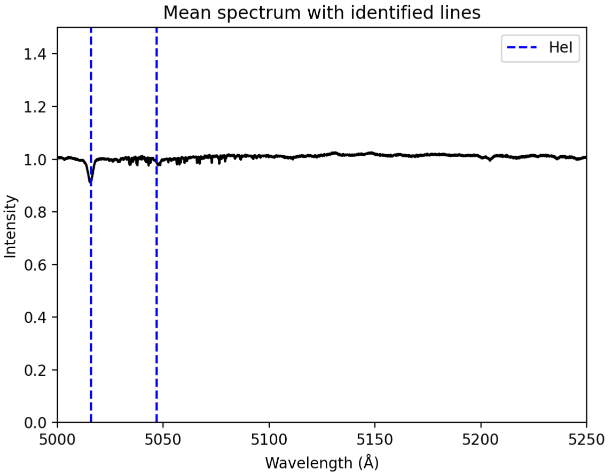

Fig. 28. 5000 to 5250 Å.

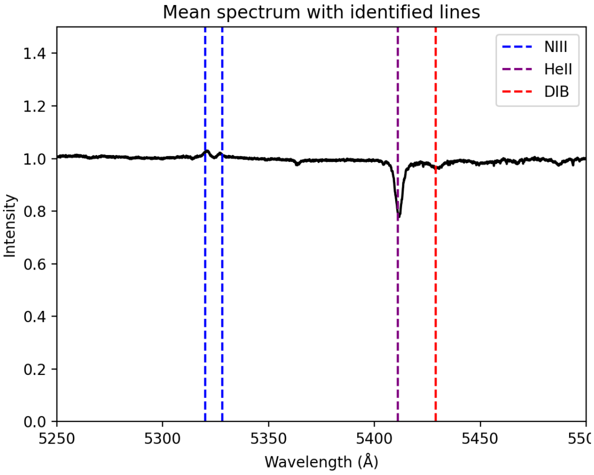

Fig. 29. 5250 to 5500 Å.

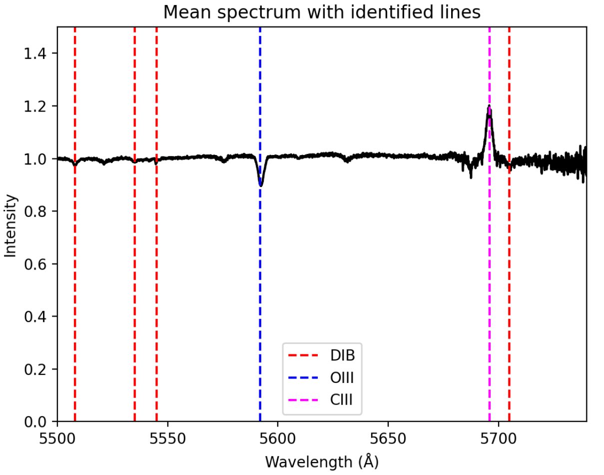

Fig. 30. 5500 to 5740 Å.

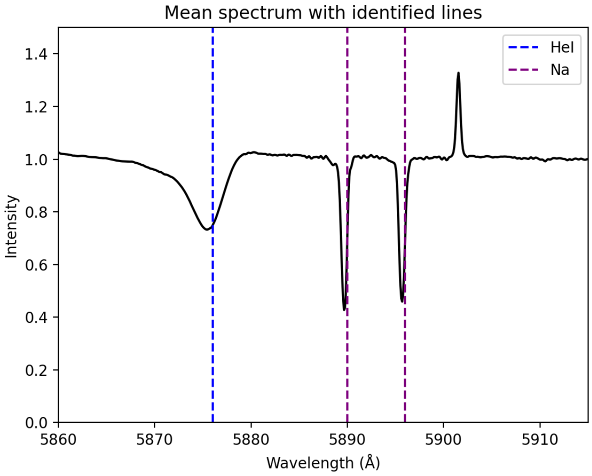

Fig. 31. 5860 to 5910 Å. Note that the emission spike near 5902 Ångstrom is an artifact resulting from the correction of the telluric lines.

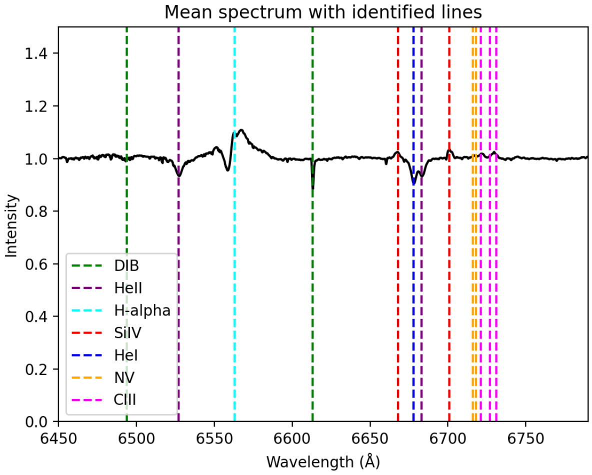

Fig. 32. 6450 to 6790 Å.

3.2.2 Radial velocities

To measure radial velocities from spectroscopic data, a spectral line must be selected and its center measured. The shift of the line center is due to the Doppler effect and allows to calculate the radial velocity r using this equation:

$$r = \frac{(x - x_{th})}{x_{th}}.c$$

with x the measured center of the line, x_{th} the theoretical center and c the speed of light.

Based on the results obtained in previous studies of the star and also on the aspect of the mean spectrum, we decided to perform the measurement of the radial velocities on a total of 5 lines to first get information about the radial velocity variability of the star. Three of those lines (He II 4200, He II 4542, He II 5412) were chosen because these He II transitions arise rather deep inside the photosphere and should not be influenced too heavily by the stellar wind. As such, the variability that could be observed would only be due to variations in the star itself (either orbital motion or pulsation). We note here that whilst the three He II lines are in absorption, Si IV is an emission line that is likely formed at the transition between photosphere and stellar wind. The last line on our list is an interstellar line (Ca II 3933), chosen to evaluate the instrumental error. The interstellar lines are significantly narrower than the stellar lines and should not undergo any variability on the timescale of our observing campaign. The dispersion of the radial velocities of these lines thus provides a direct indication of the stability and accuracy of the wavelength calibration of our spectra.

In the following figures (Figs. 33 to 37) the radial velocities of each chosen line are represented as a function of time expressed in HJD-2459000. It is easy to notice that the Ca II 3933 line shows less variation than the others. This is expected as the Calcium line is formed in the interstellar medium whilst the others arise in the photosphere of the star.

Table 3.3: Characteristics of the radial velocities

Line	r mean value km/s	r standard deviation km/s	x_{th} Å
He II 4200	-0.036	0.499	4199.83
He II 4542	-1.50	0.385	4541.59
He II 5412	3.21	0.562	5411.52
Ca II 3933	-11.6	0.052	3933.64
Si IV 6701	5.36	0.668	6701.21

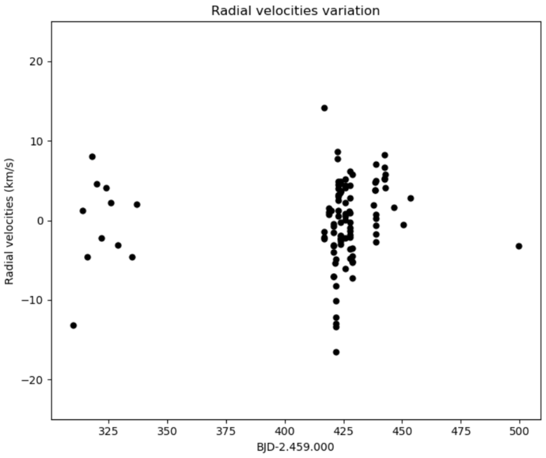

Fig. 33. Radial velocity variations for He II 4200.

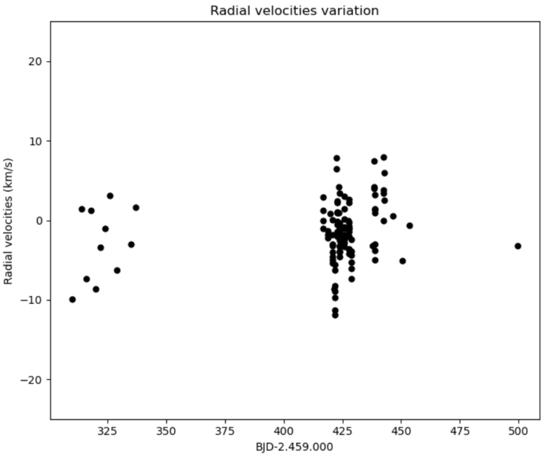

Fig. 34. Radial velocity variations for He II 4542.

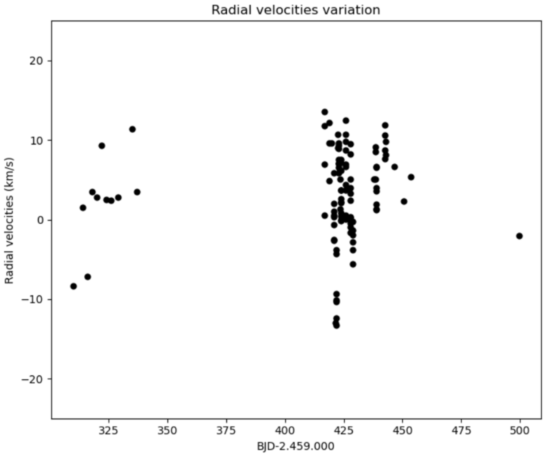

Fig. 35. Radial velocity variations for He II 5412.

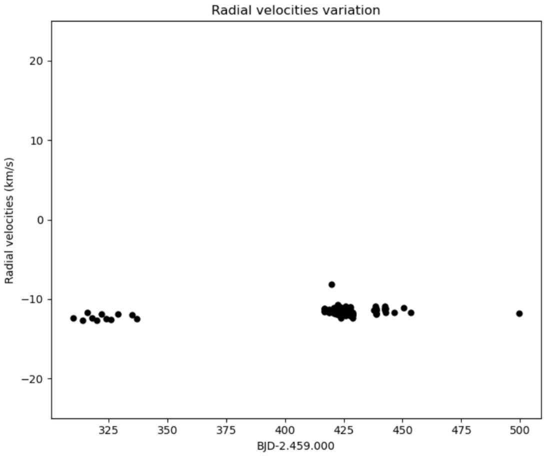

Fig. 36. Radial velocity variations for Ca II 3933.

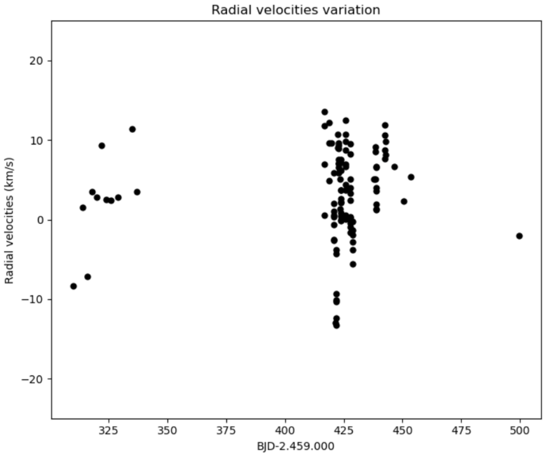

Fig. 37. Radial velocity variations for Si IV 6701.

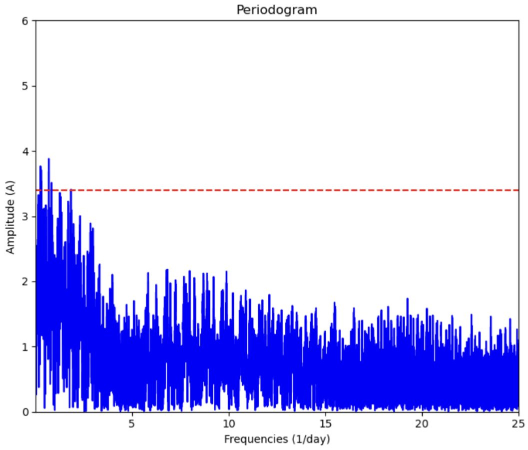

Fig. 38. Periodogram of the radial velocities for He II 4200.

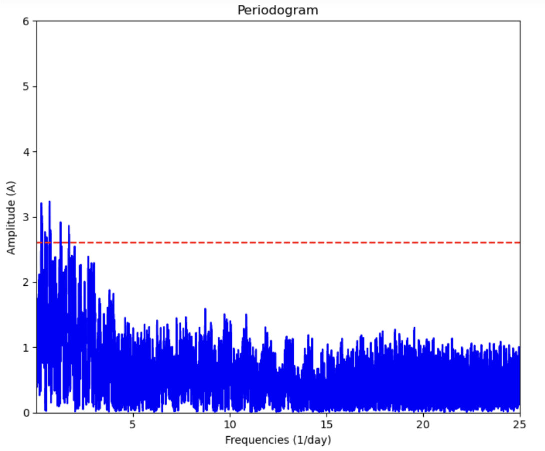

Fig. 39. Periodogram of the radial velocities variations for He II 4542.

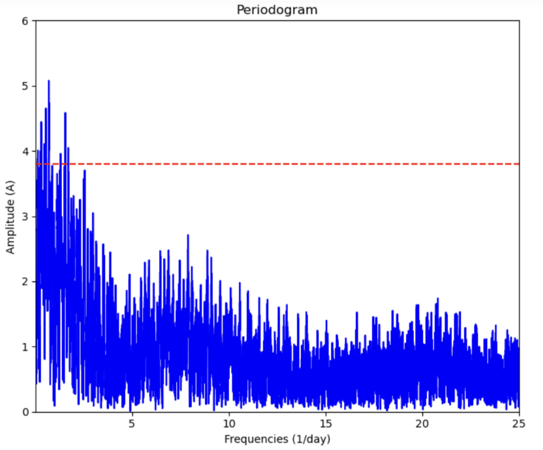

Fig. 40. Periodogram of the radial velocities for He II 5412.

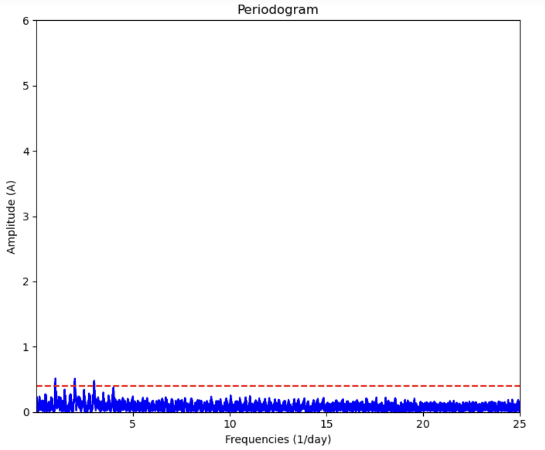

Fig. 41. Periodogram of the radial velocities for Ca II 3933.

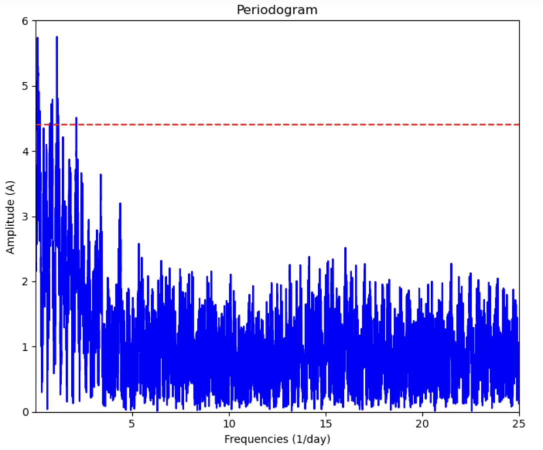

Fig. 42. Periodogram of the radial velocities for Si IV 6701.

A Fourier analysis was performed on the time series of radial velocities to search for possible periodic variations. The parameters chosen for this analysis were decided in the same way as outlined in the photometric part 3.1.2. The lowest frequency came from the total time spent to acquire the spectrometric data, 189 days, which corresponds to a peak width of about $5 * 10^{-3}$ day^{-1}. The step in frequency was of $5 * 10^{-4}$ day^{-1} and the highest frequency was chosen using the Nyquist frequency for the shortest time between two acquisitions: about 25 day^{-1}. While those values are theoretically the best to use in a set of data, in this case, because of the large gaps in the time series spanning more than a month and the gaps due to the daytime, they are not ideal.

Unfortunately, no noise model could be fitted on those periodograms. The one used previously in the photometric section is not suited to this case. Indeed, no clear noise shape (red, white, red+white) could be distinguished in the log-logarithmic periodograms. This is at least partly due to the aliasing problem that strongly impacts our spectroscopic time series. An example is provided in Fig.43.

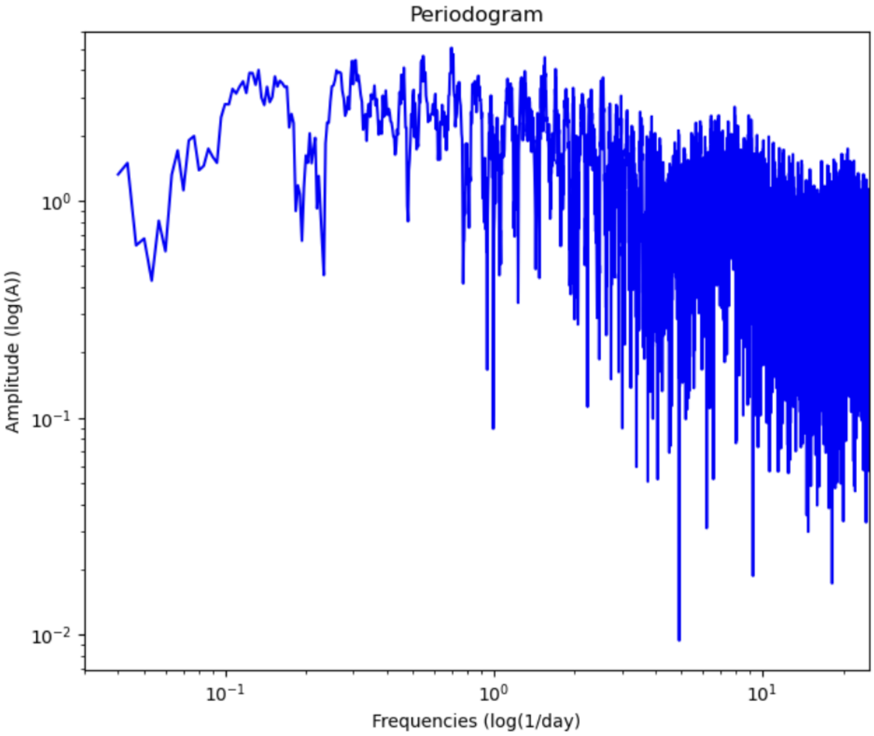

Fig. 43. Periodogram for the 5412 line, in logarithmic scale.

As no noise model could be fitted on those periodograms, another method had to be used to derive a meaningful significance level: shuffling. This consists in randomly mixing the 108 pairs of times and radial velocities and performing a Fourier analysis of the newly created artificial time series. This process was repeated a thousand times and the amplitude of the highest peak in the Fourier spectrum was recorded. For each of the spectral lines, we then build the distribution of these peak amplitudes. The shape of these distributions allows us to determine a 1% significance level: any amplitude higher than this level has only a 1% chance that it could be due to random fluctuation. The results are shown in Fig.44.

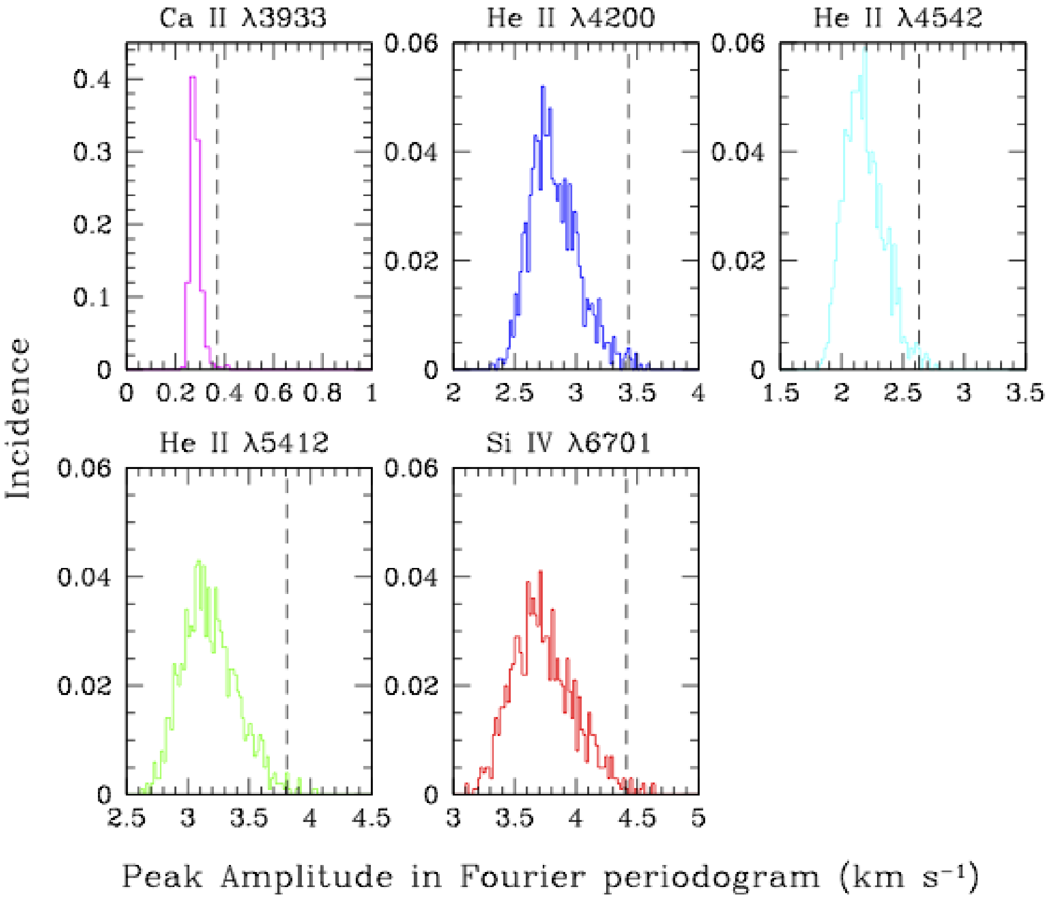

Fig. 44. Distribution of amplitude of the strongest peaks in the Fourier periodograms of the reshuffled time series. The dashed vertical lines yield the 1% significance level.

The 1% significance levels that were determined in this way amount to 3.4 km/s for He II 4200, 2.6 km/s for He II 4542, 3.8 km/s for He II 5412, 4.4 km/s for Si IV 6701 and 0.4 km/s for Ca II. The majority of the low-frequency($<$ 3 per day) peaks that we observe in our periodograms are above these thresholds and thus indicate significant variability.

Figures 38 to 42 display the different periodograms, with a red line corresponding to the threshold obtained using the shuffling method. In every graphics, multiple peaks are above them and are thus found to be significant.

3.2.3 Temporal Variance Spectrum

Another test can provide further information about the spectroscopic variations: the Temporal Variance Spectrum (Fullerton, A. W., Gies, D. R., and Bolton, C. T. 1996). This method allows the user to quantify the significance of line-profile variations. Measuring the error on the continuum of each spectrum allows us to build a mean error and assign weight w_i.

$$\sigma_0^2 = (\frac{\Sigma\sigma_i^{-2}}{N})^{-1}$$

$$w_i = (\frac{\sigma_O}{\sigma_i})^2$$

Here, σ_0 is the mean error, σ_i the error of spectrum number i, N the number of spectra and w_i the weight of the spectrum number i. The squared mean error is $\sigma_0^2 = 1.734 * 10^{-4}$ in our cases. This value is unique as there is only one continuum error for each blue spectrum. We choose to use the blue squared mean error for the red spectra too as it gives a stricter threshold (the blue spectra having a lower SNR, the threshold created using it is higher and stricter). This does not mean that we lose information about significant signal in the red spectra: Hα and He I 5876 are stronger and have clearer line profile variations than the selected blue lines. This means that each spectrum has only one weight unrelated to which line is analyzed. From there a weighted mean spectrum can be constructed and a residual matrix built.

$$\bar{S_j} = \frac{\Sigma w_i S_{ij}}{N}$$

$$d_{ij} = S_{ij} - \bar{S_j}$$

With S_{ij} the value of the i^{th} spectrum at the wavelength j, $\bar{S_j}$, the weighted mean spectrum at each wavelength value and d_{ij} the ij element of the residual matrix. It is easily seen that the rows of the residual matrix contain the differences between the spectrum and the weighted mean, whilst the columns yield the variations at a specific wavelength.

Starting from this residual matrix, a weighted residual matrix D_{ij} can be constructed and the TVS calculated from it.

$$D_{ij} = \sqrt{w_i/\alpha_{ij}}d_{ij}$$

$$(TVS)_j = (\Sigma_{i=1}^{N} D_{ij}^2)/(N-1)$$

With $\alpha_{ij} = S_{ij}$ in this case. Further details on this method can be found in Fullerton, A. W., Gies, D. R., and Bolton, C. T. 1996 who first proposed it. As in that paper, the significance threshold is fixed at $\sigma_0^2\chi_{N-1}^2$ where χ_{N-1}^2 stands for the χ^2 distribution with $N-1$ degrees of freedom and evaluated for a 1% level. In our case, the corresponding threshold is $2.3326 * 10^{-4}$. As it is based on the squared mean error, its value is also unique and common to all the TVS.

In Figs. 45 to 49, we can see the different Temporal Variance Spectra that have been constructed, with the threshold in red:

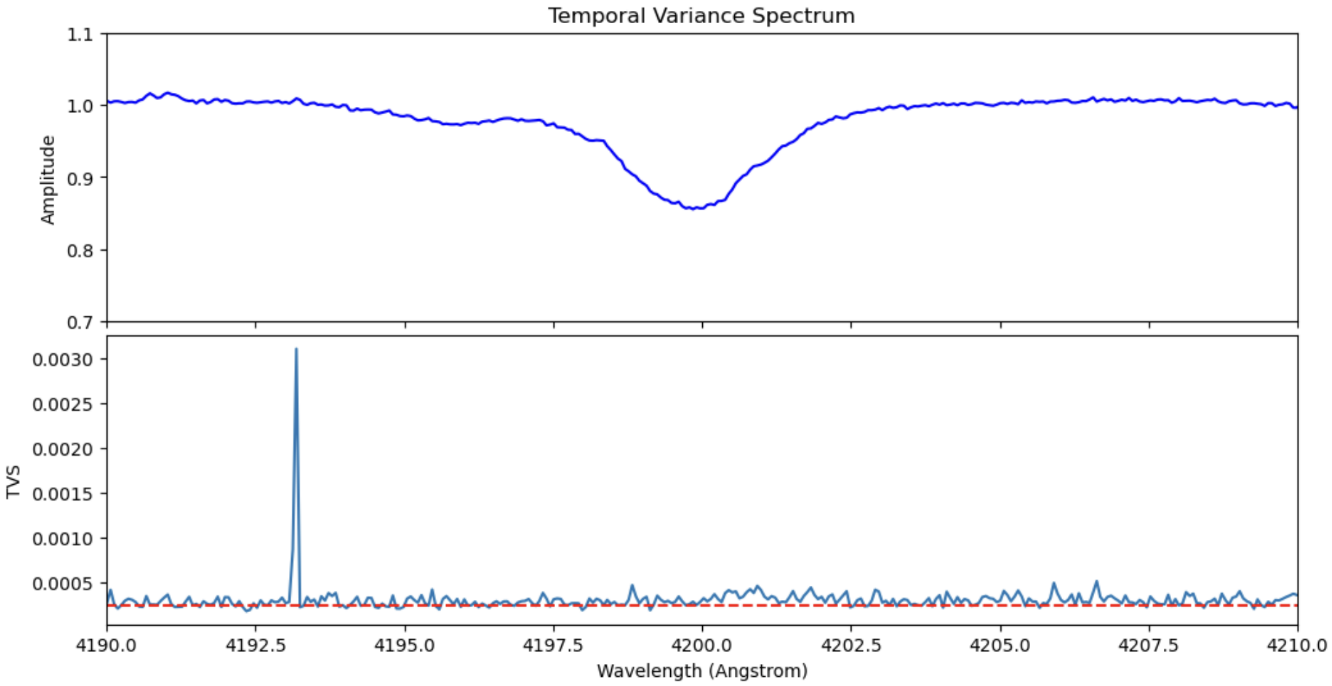

Fig. 45. Above: He II 4200 line; below: TVS of He II 4200.

From those graphics, multiple things can be deduced. The first is that none of them shows significant variability except He II 5412. In principle, the threshold for significant variations should be close to the continuum level. The small differences reflect small imperfections during the normalization. That should be the case for He II 5412. The peaks in He II 4200 and 5412 are due to cosmic rays. The overall TVS show a stochastic variability, similar to noise.

In Ca II 3933 case, the variations on the line (3933-3934 Å) can be explained. As the line is very thin (width less than two Å) and the sampling is 0.09 Å. As there are only two or three points around the center position, it is easy for it to be in a different pixel on another night. This creates an artificial variation visible on the TVS.

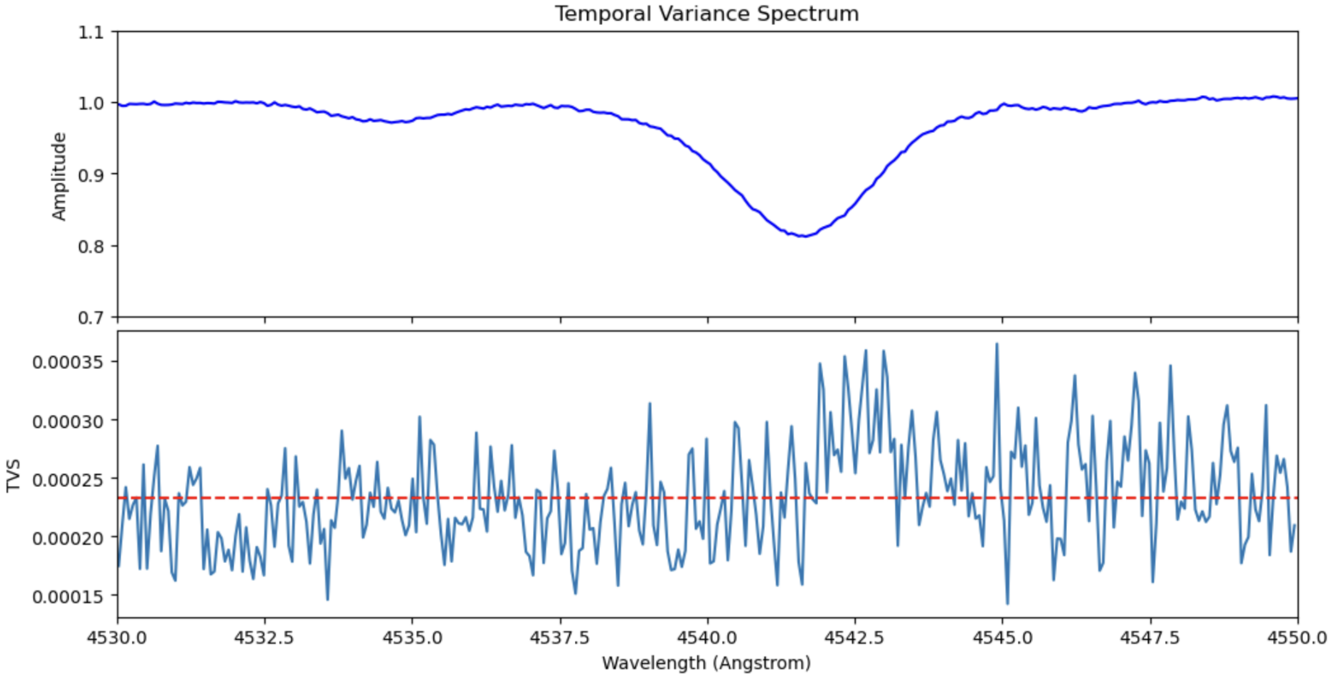

Fig. 46. Above: He II 4542 line; below: TVS of He II 4542.

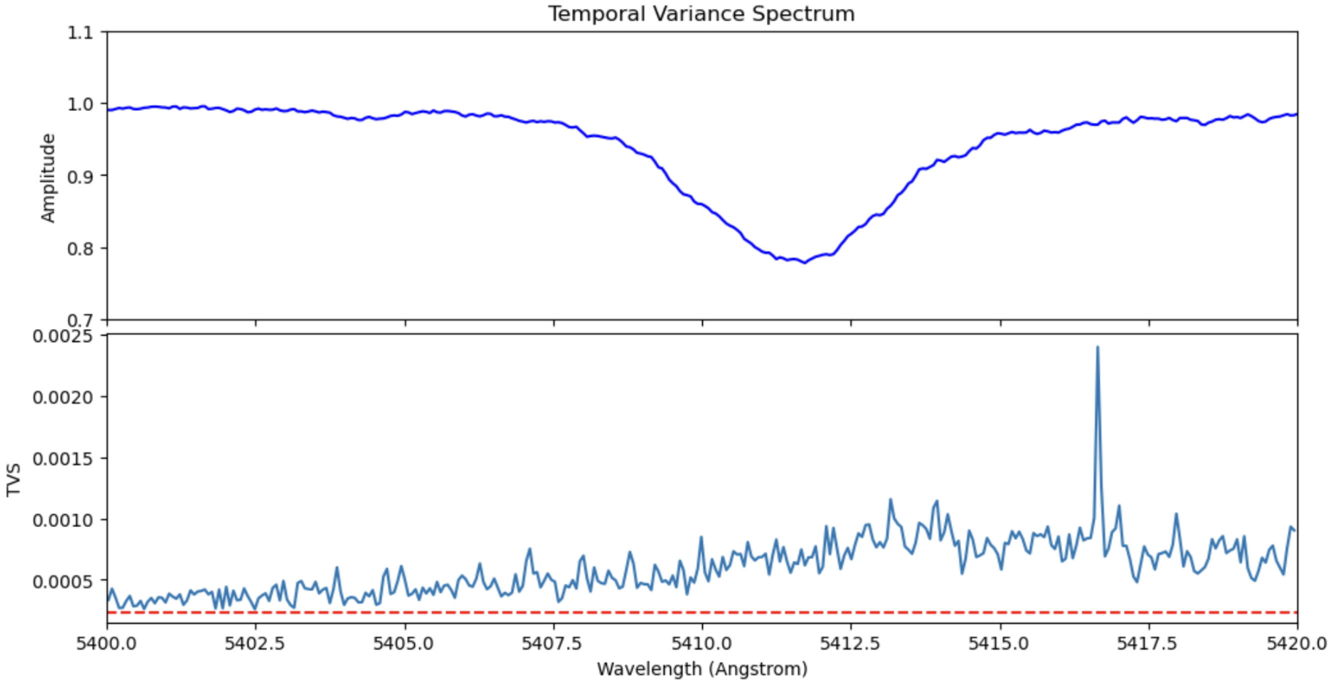

Fig. 47. Above: He II 5412 line; below: TVS of He II 5412.

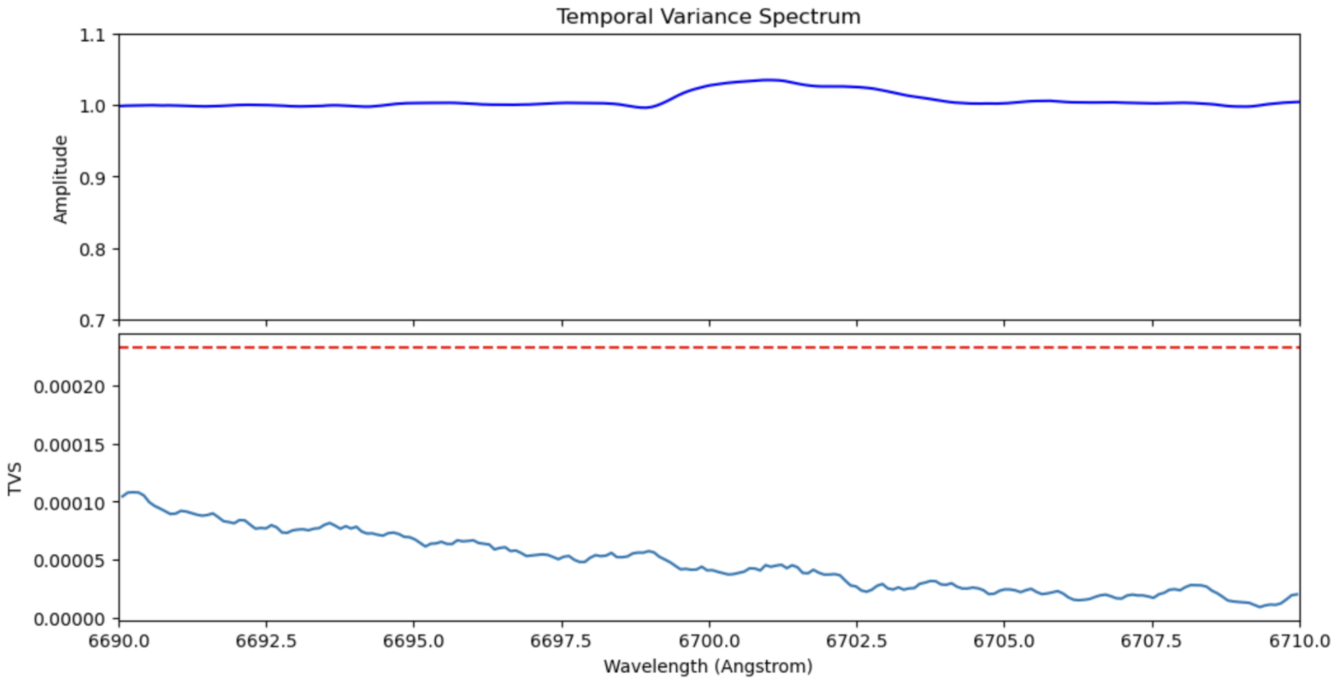

Fig. 48. Above: Si IV 6701 line; below: TVS of Si IV 6701.

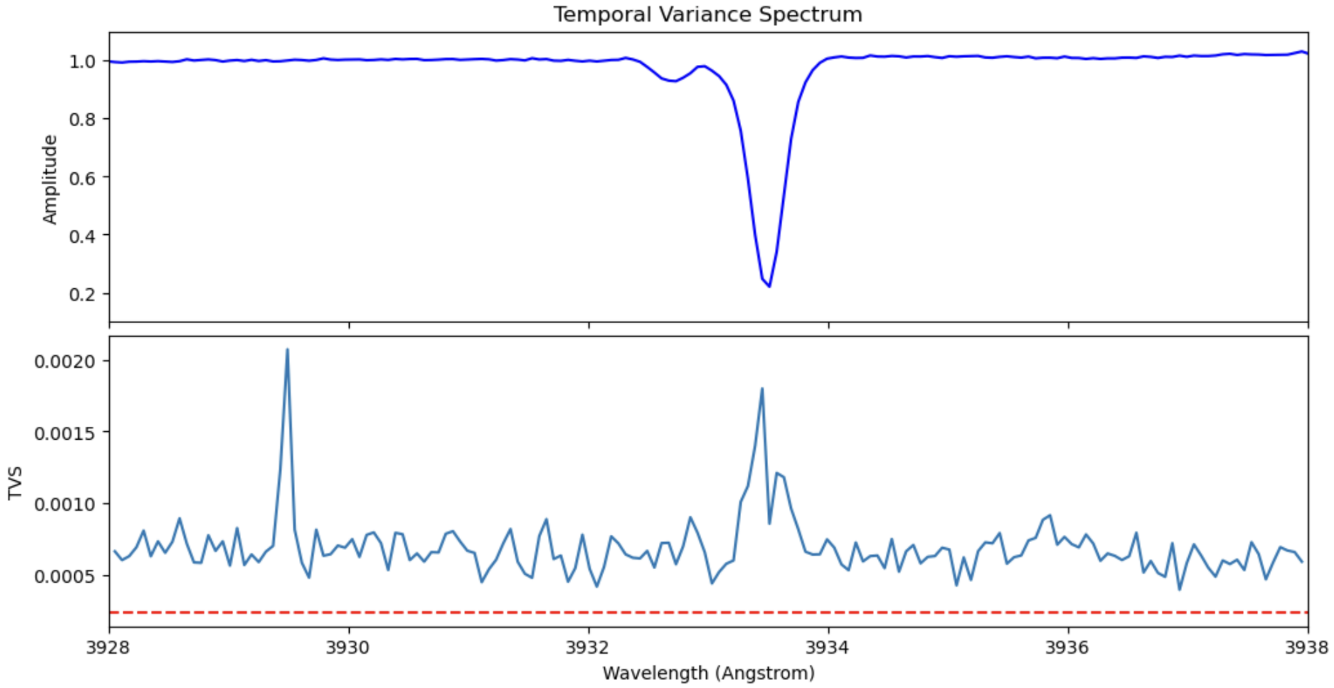

Fig. 49. Above: Ca II 3933 line; below: TVS of Ca II 3933.

3.2.4 Wind spectral lines

The previously studied spectral lines were lines produced in the photosphere of the star, except for Ca II which is an interstellar line. To understand the behaviour of the surrounding of the star, other lines must be observed. In this case, Hα, Hβ, Hγ, He I 5876 and He II 4686 were chosen. Those lines are particularly interesting to study as previous studies showed that wind lines are those which exhibit the strongest signature of the 4.76 day modulation.

Those lines are from the same spectra as the previous ones, meaning that the correction were the same and the errors on the spectra were the same too. As such, it is easy to construct their TVS. Figures 50 to 54 show the TVS of the different lines. We can notice that the amplitude of the variations is much more important than in the TVS of the previous lines. The level of the TVS is now in all cases much higher than the 1% significance level, indicating a truly significant variability.

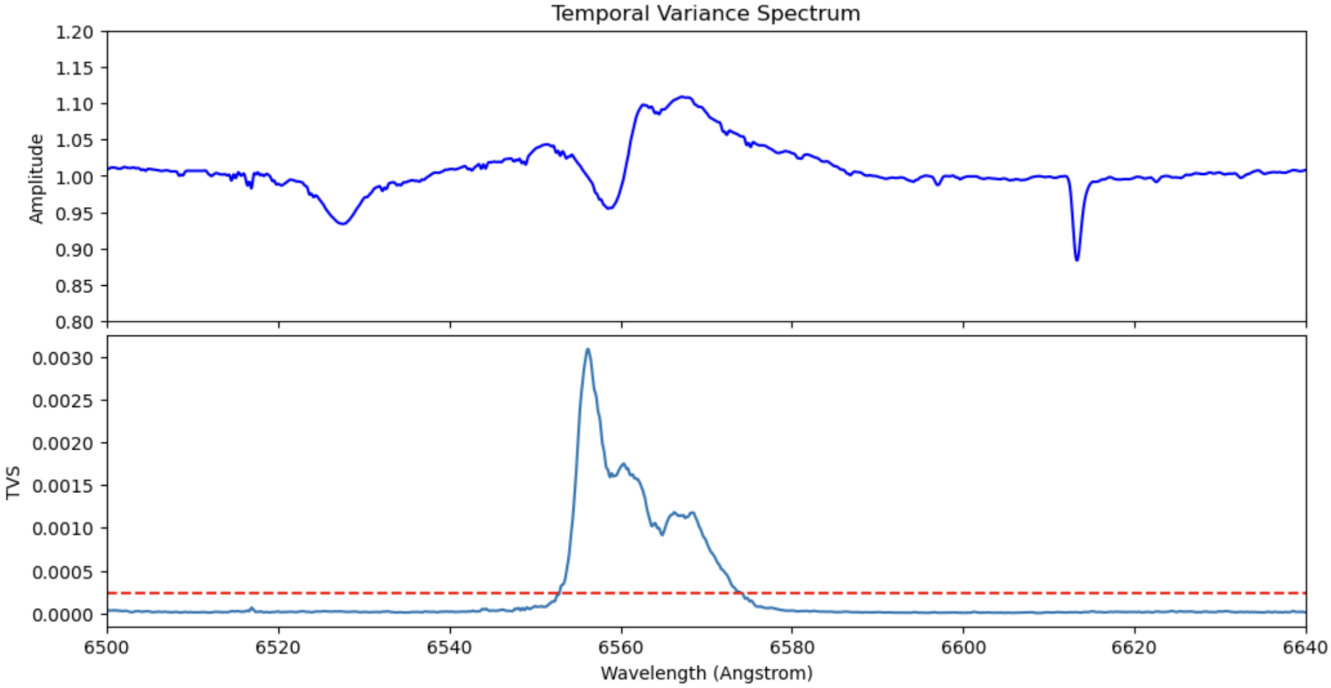

Fig. 50. Above: Hα line; below: TVS of Hα

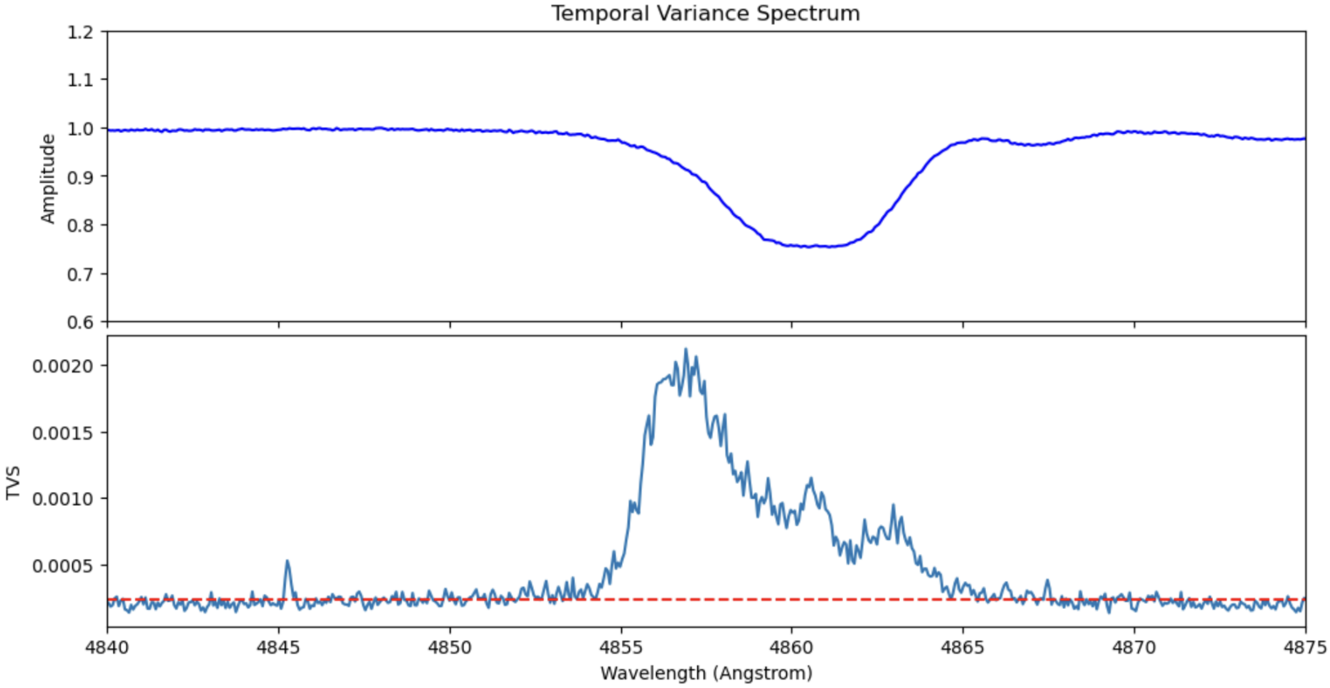

Fig. 51. Above: Hβ line; below: TVS of Hβ

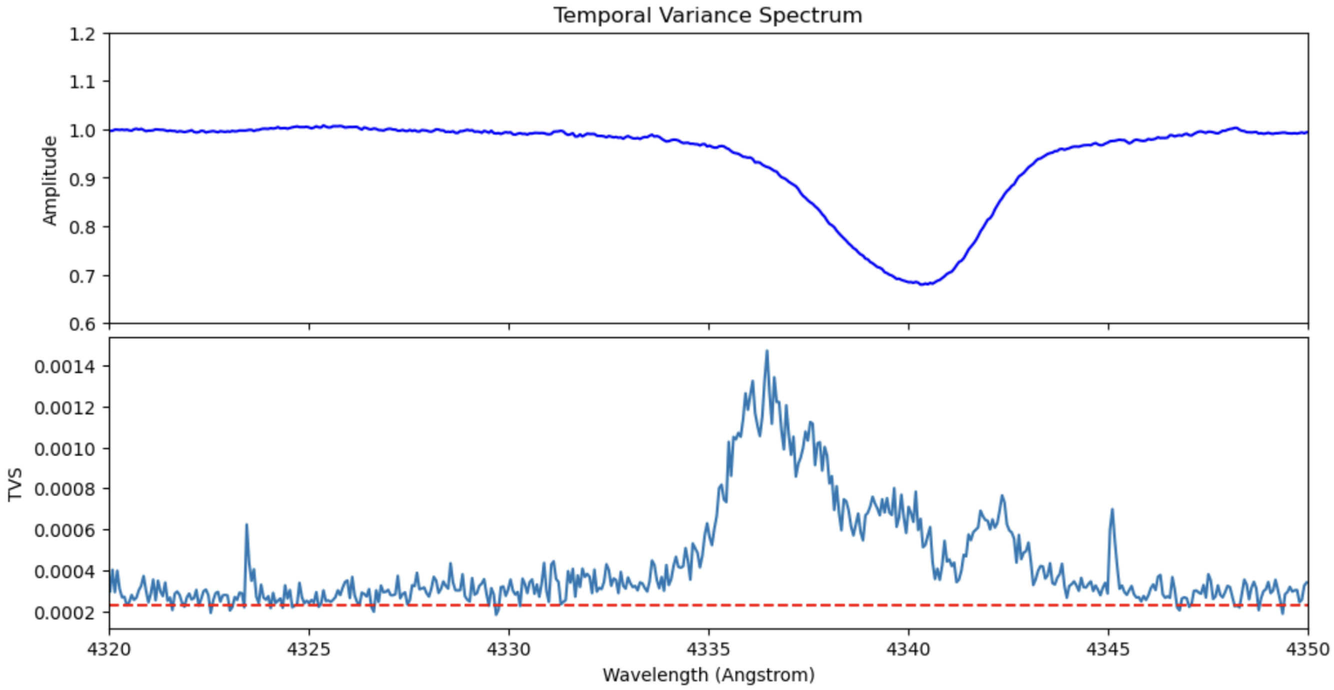

Fig. 52. Above: Hγ line; below: TVS of Hγ

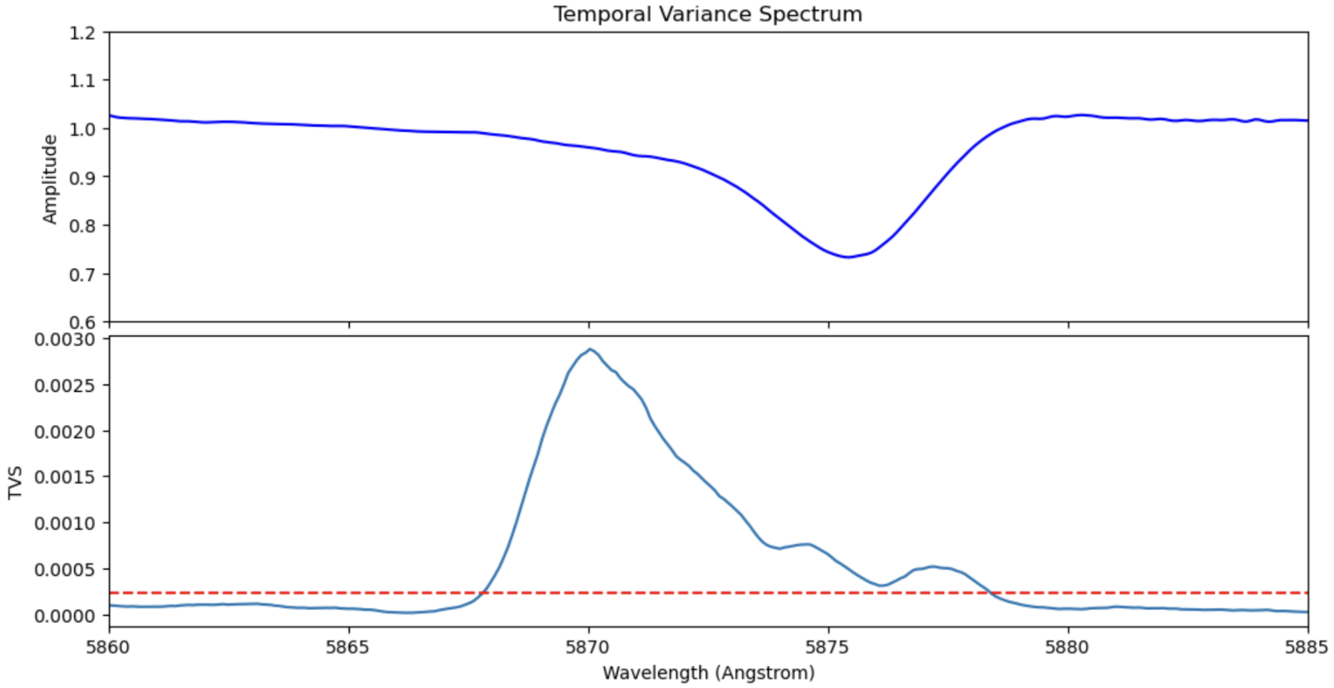

Fig. 53. Above: He I 5875 line; below: TVS of He I 5875

As before, we perform a Fourier analysis. In this case instead of selecting the radial velocity of the line to perform the analysis, we analyze each wavelength bin within the width of the profile. It is necessary as the whole line profile changes with time and the P-Cygni profiles cannot be given a precise center.

The results are displayed as 2-dimensional Fourier periodograms: the abscissa yields the wavelength, the ordinate is the frequency and the level of the periodogram is represented by a gradient in color. In Figs. 55 to 59, we can see the different results for those lines.

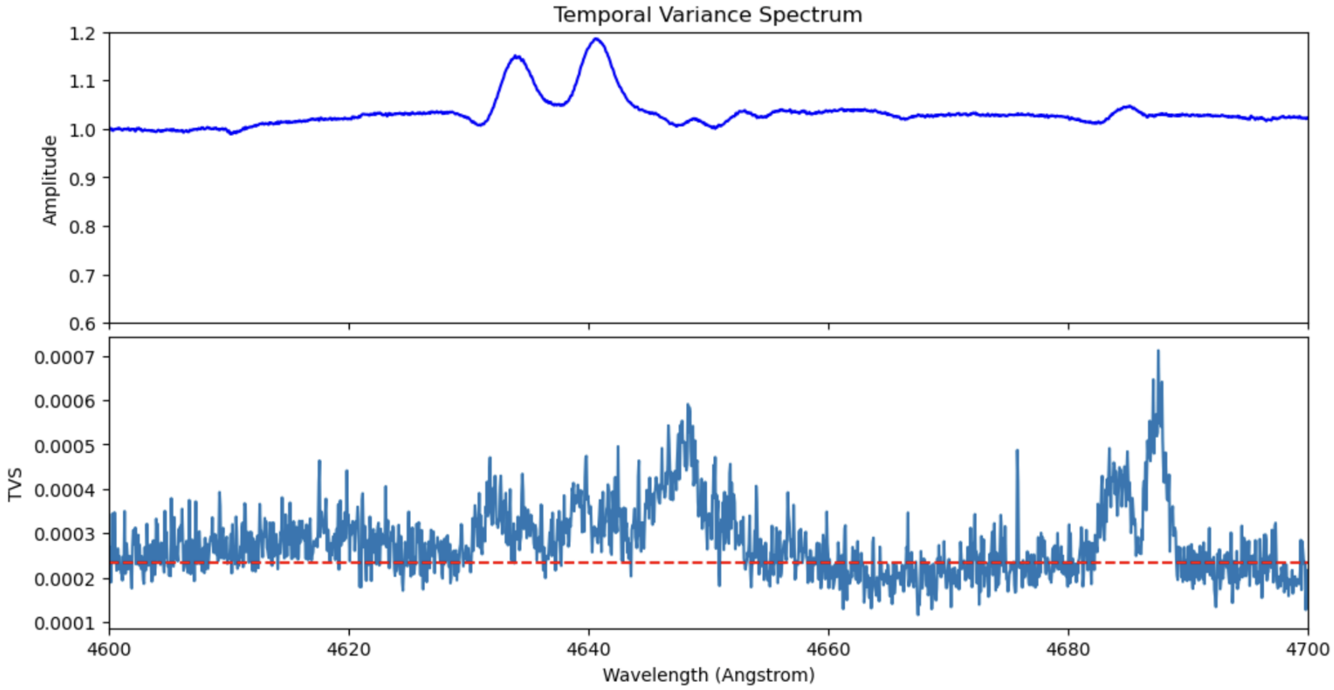

Fig. 54. Above: C III 4647-51 and He II 4686 lines; below: TVS of C III 4647-51 and He II 4686

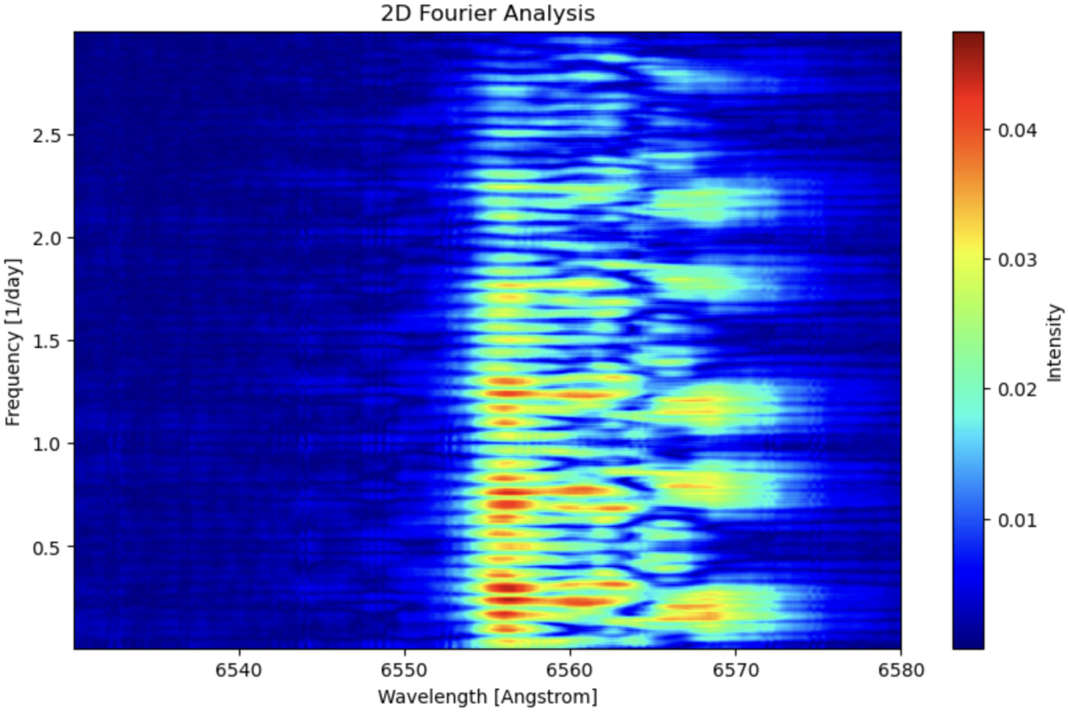

Fig. 55. Fourier 2-D of Hα.

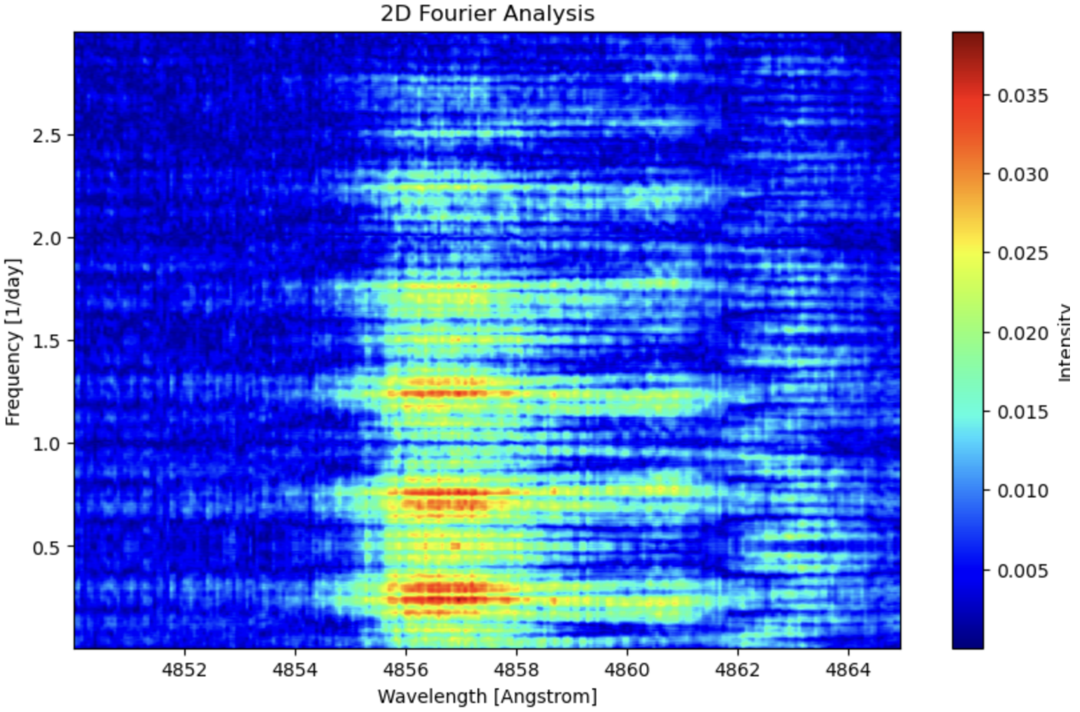

Fig. 56. Fourier 2-D of Hβ.

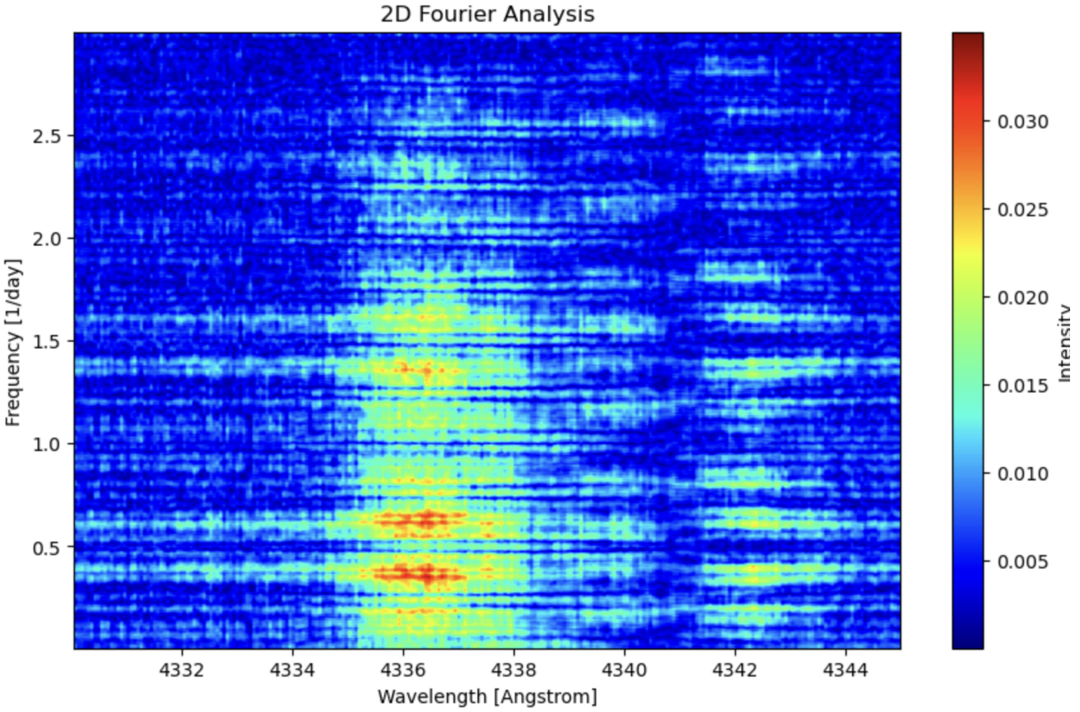

Fig. 57. Fourier 2-D of Hγ.

As before, we will try to establish a threshold. Two different approaches were considered. The first was based on the same shuffling method previously applied to other spectrometric data. The shuffling was applied to timeseries for specific wavelength bins, thereby sampling different levels of the TVS.

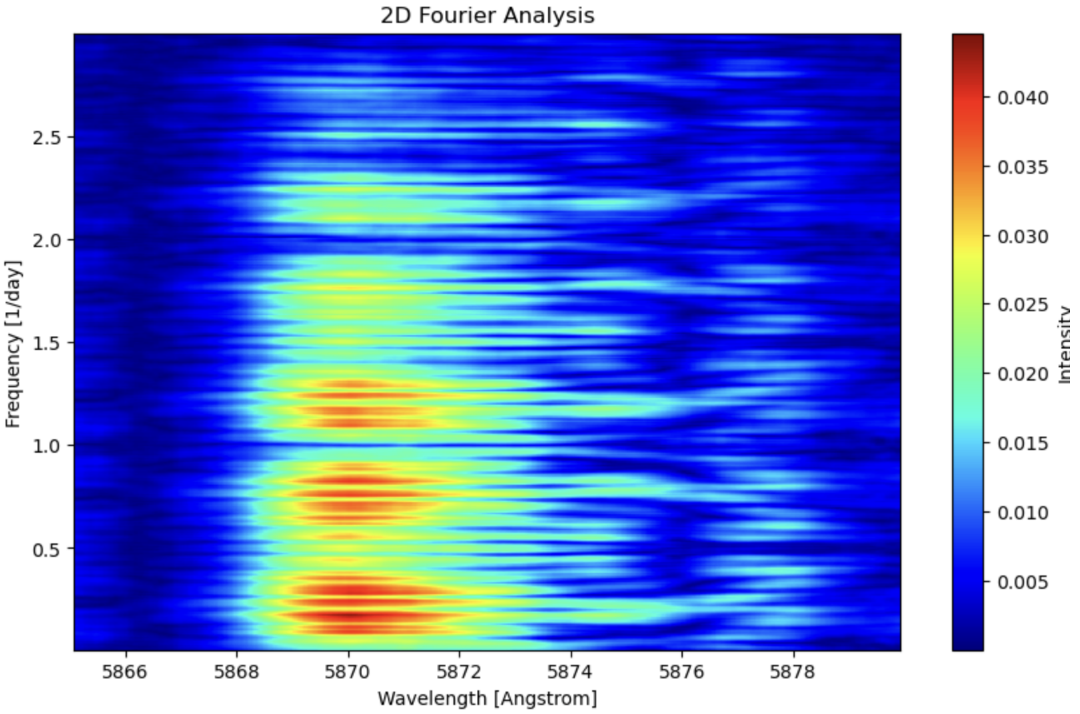

Fig. 58. Fourier 2-D of He I 5876.

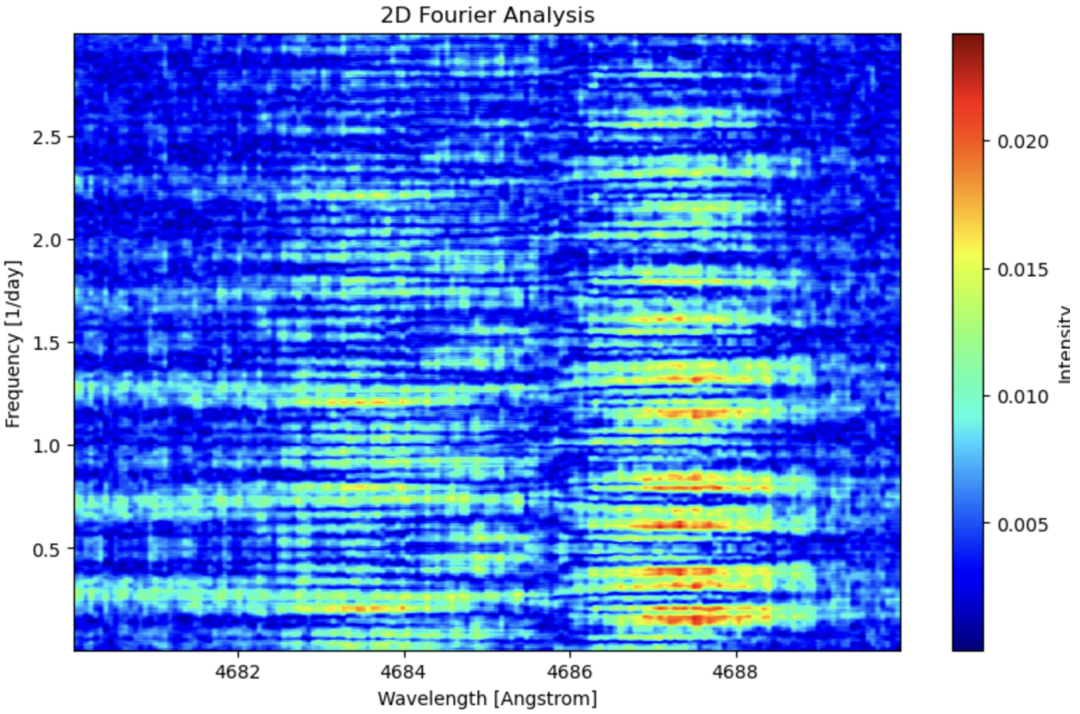

Fig. 59. Fourier 2-D of He II 4686.

This allowed us to derive a simple linear scaling relation between the 1% significance level and the value of TVS$^{1/2}$. This relation, observed in Fig. 60, was then used to infer the significance level for each wavelength based on the associated value of the TVS. The Hα was used for the red spectra and the Hβ for the blue spectra. This approach yields a rather strict significance threshold.

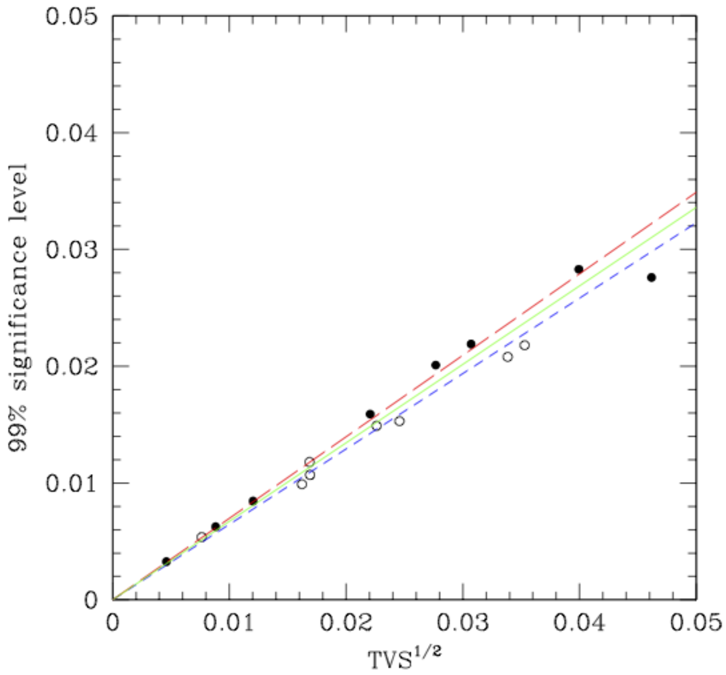

Fig. 60. The figure now displays the Hα data points (filled circles) and Hβ data points (open circles), along with the best-fit lines for all Hα (red line), Hβ points (blue line), and their combined dataset (green line). The corresponding relations are: $\text{Threshold}_{H\alpha} = (0.699 \pm 0.039) * TVS^{1/2}$ $\text{Threshold}_{H\beta} = (0.645 \pm 0.036) * TVS^{1/2}$.

The second method was to use a threshold based on the mean noise. For this purpose, we selected a region of the 2-D Fourier periodograms without any visible significant signal, calculated the average noise, and considered a threshold of 5 times this calculated average.

In both cases, we subtracted to zero all the points under the threshold, leaving only significant signal. The 2-D analysis using the TVS threshold can be seen in Figs. 61 to Fig. 65,while the 2-D analysis using the mean noise threshold is shown in Figs. 66 to Fig. 70.

The first thing to notice is that all the 2-D Fourier analysis with either threshold show a main peak in intensity at about 0.21 day^{-1} as well as its aliases. The second is the actual strictness of each threshold. It seems that the TVS scaling threshold is stricter than the mean noise threshold for He I 5876. The two methods look equivalent for Hα. And finally, the mean noise method seems to be more strict for Hβ, Hγ, and He II 4686.

This differences can be explained by the different noise levels between the blue spectra and the red spectra. As mentioned in section 3.2.3, the red spectra have a lower noise level. This results in a clearer signal after Fourier transform, with higher intensity and lower noise. If the noise in the Fourier transform is lower, the resulting threshold will also be lower. This explain the big difference in the results of He I 5876 as they are the less noisy spectra. The TVS scaling threshold, not impacted by the noise in the 2-D Fourier transform, should be more "stable".

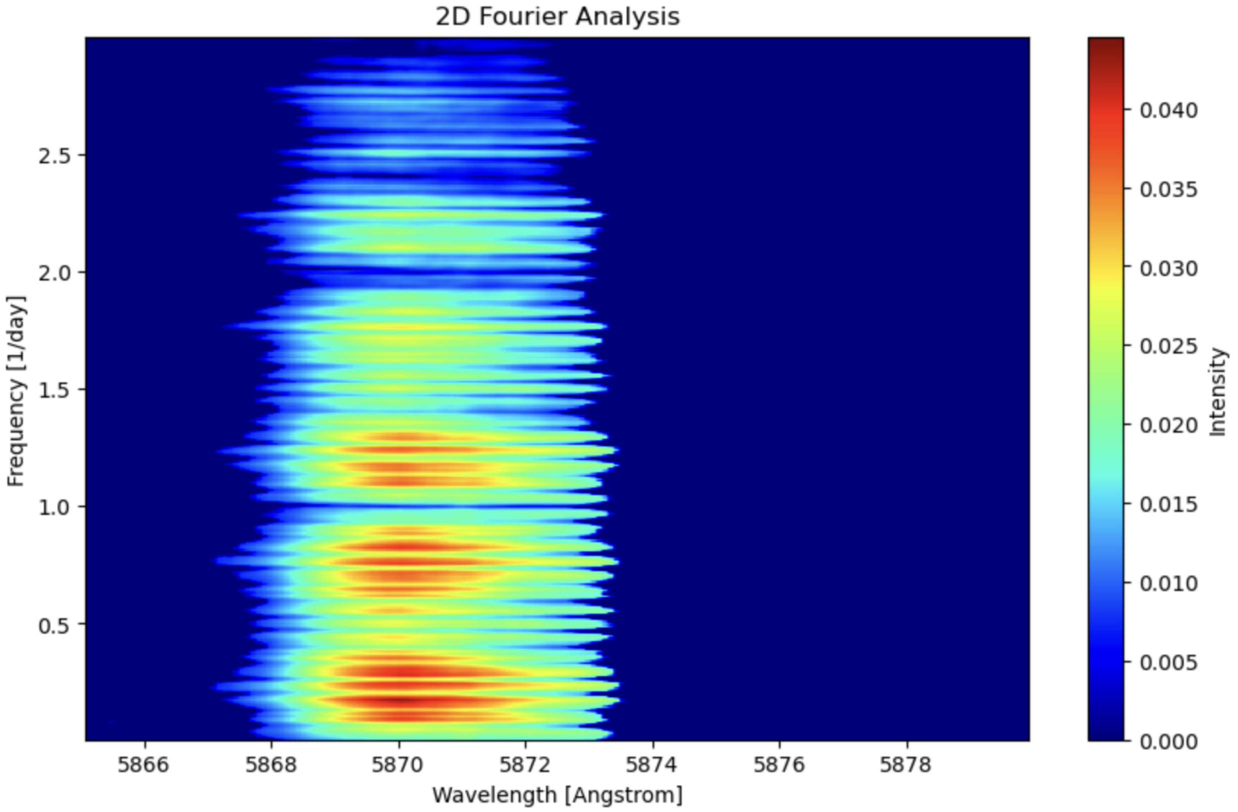

Fig. 61. Fourier 2-D of He I 5876 with a threshold scaling with the TVS$^{1/2}$.

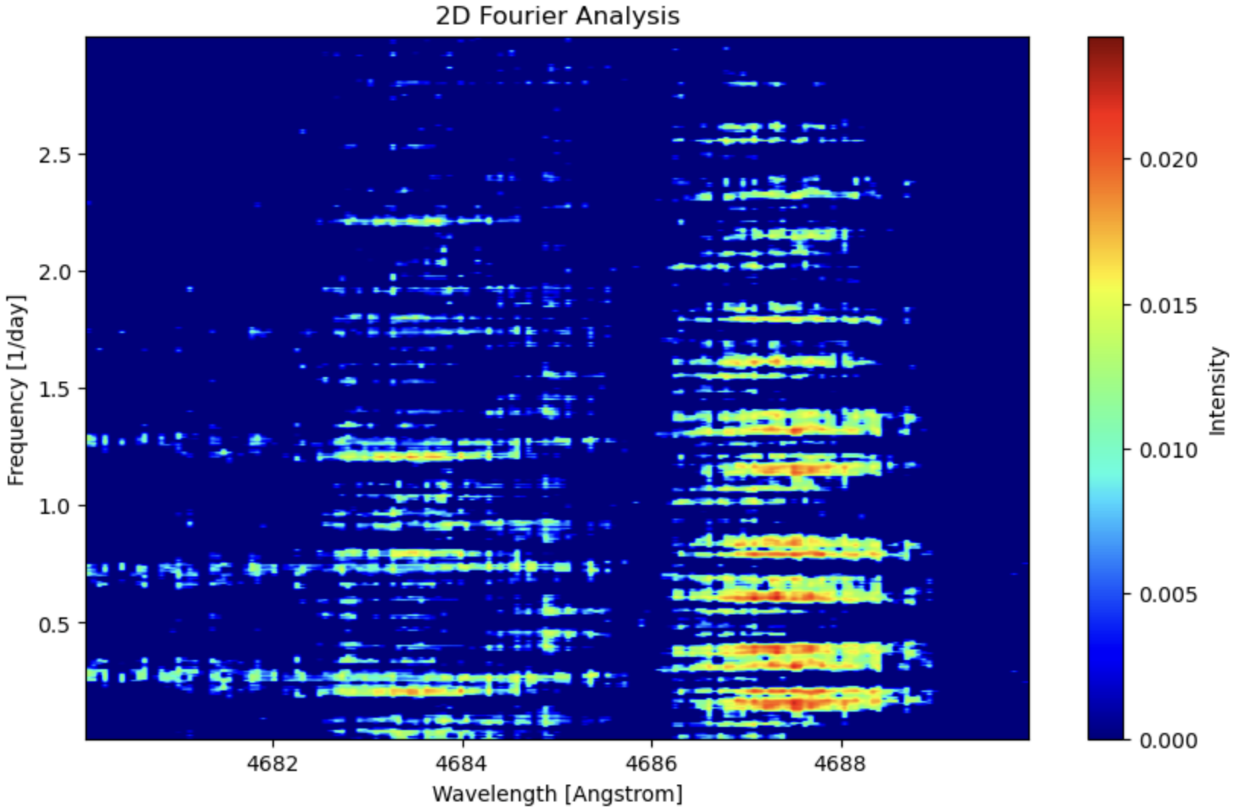

Fig. 62. Fourier 2-D of He II 4686 with a threshold scaling with the TVS$^{1/2}$.

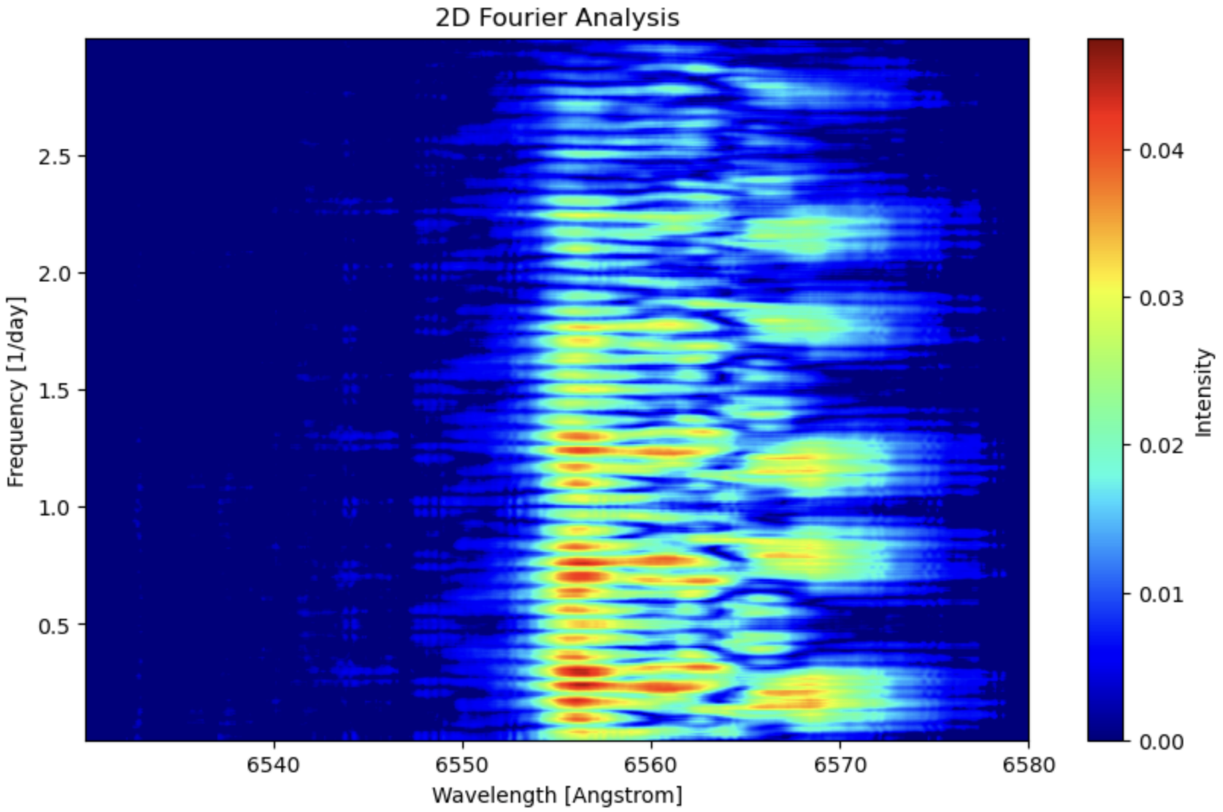

Fig. 63. Fourier 2-D of Hα with a threshold scaling with the TVS$^{1/2}$.

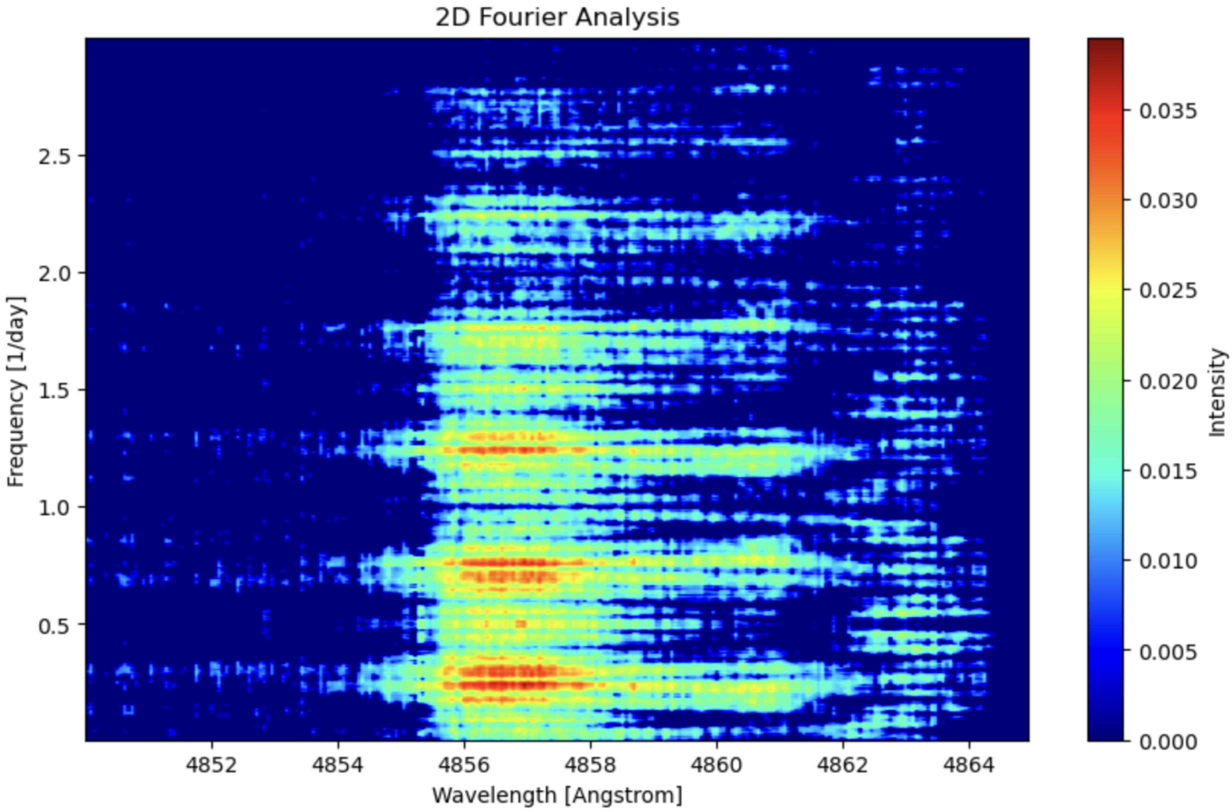

Fig. 64. Fourier 2-D of Hβ with a threshold scaling with the TVS$^{1/2}$.

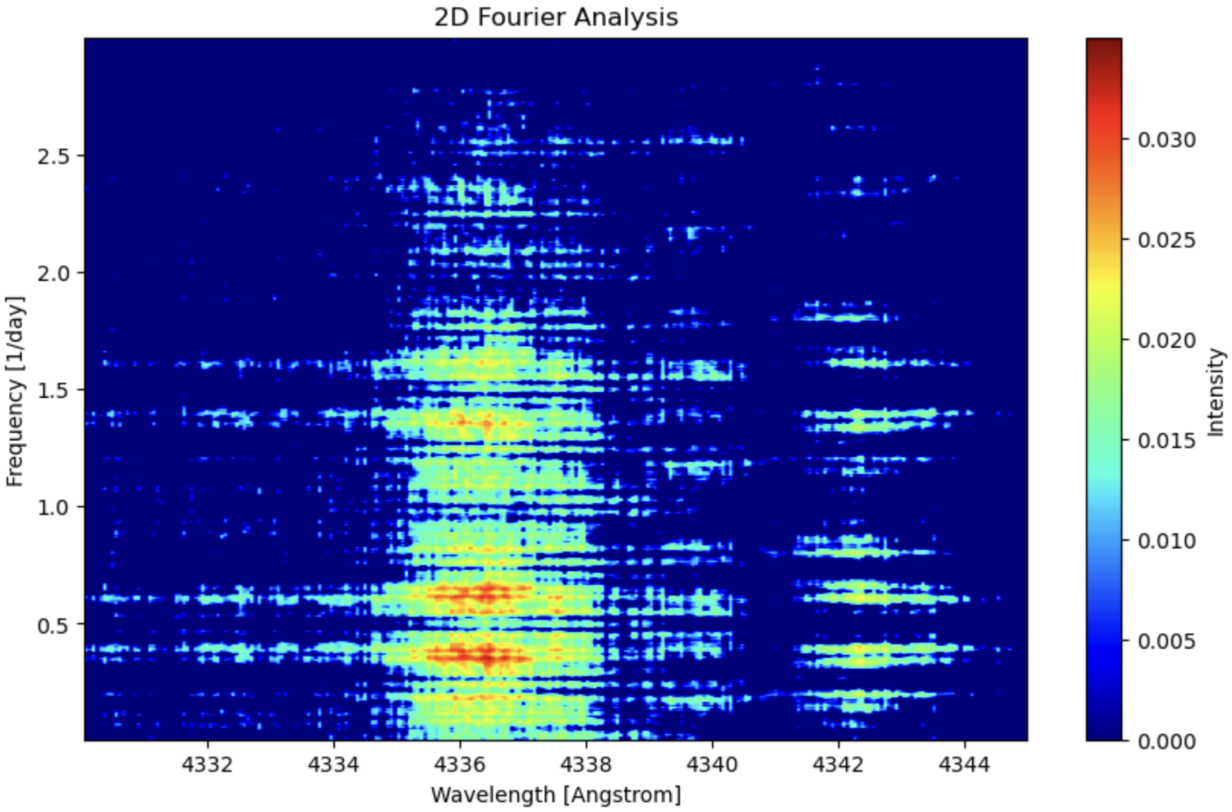

Fig. 65. Fourier 2-D of Hγ with a threshold scaling with the TVS$^{1/2}$.

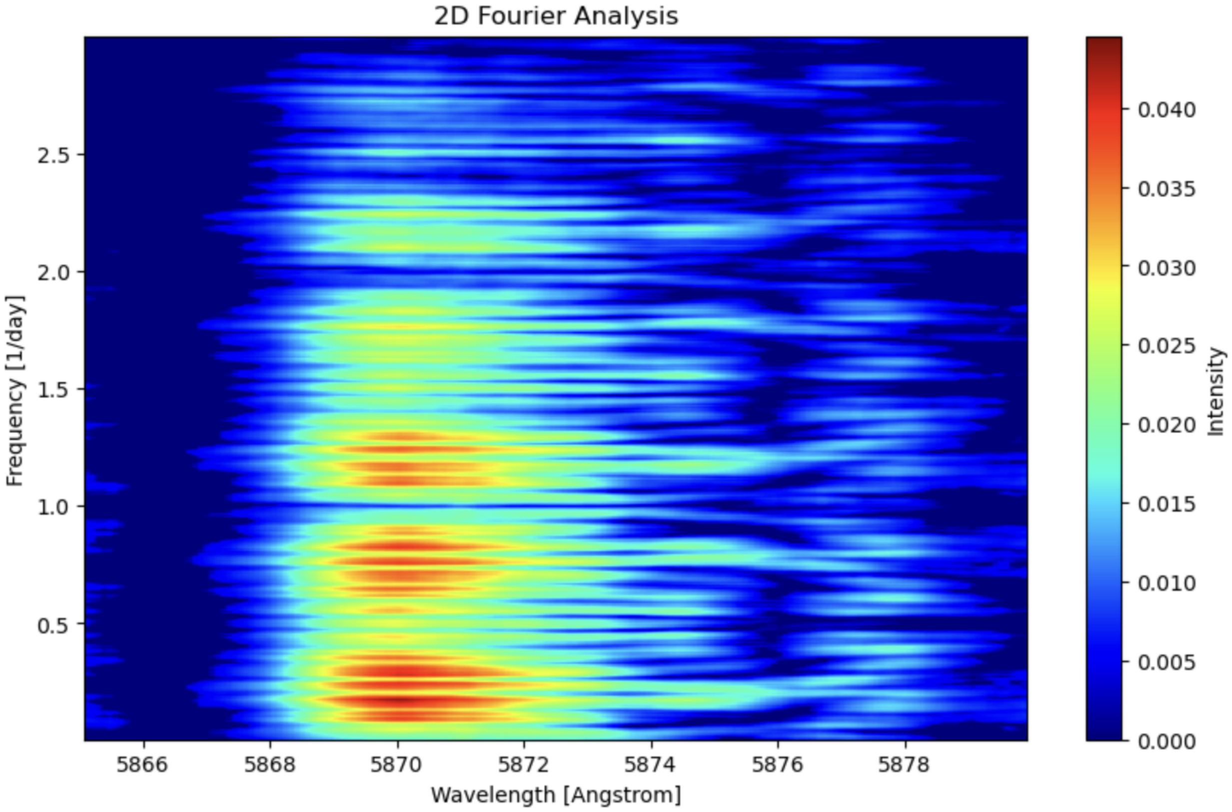

Fig. 66. Fourier 2-D of He I 5876 with a threshold based on the mean noise.

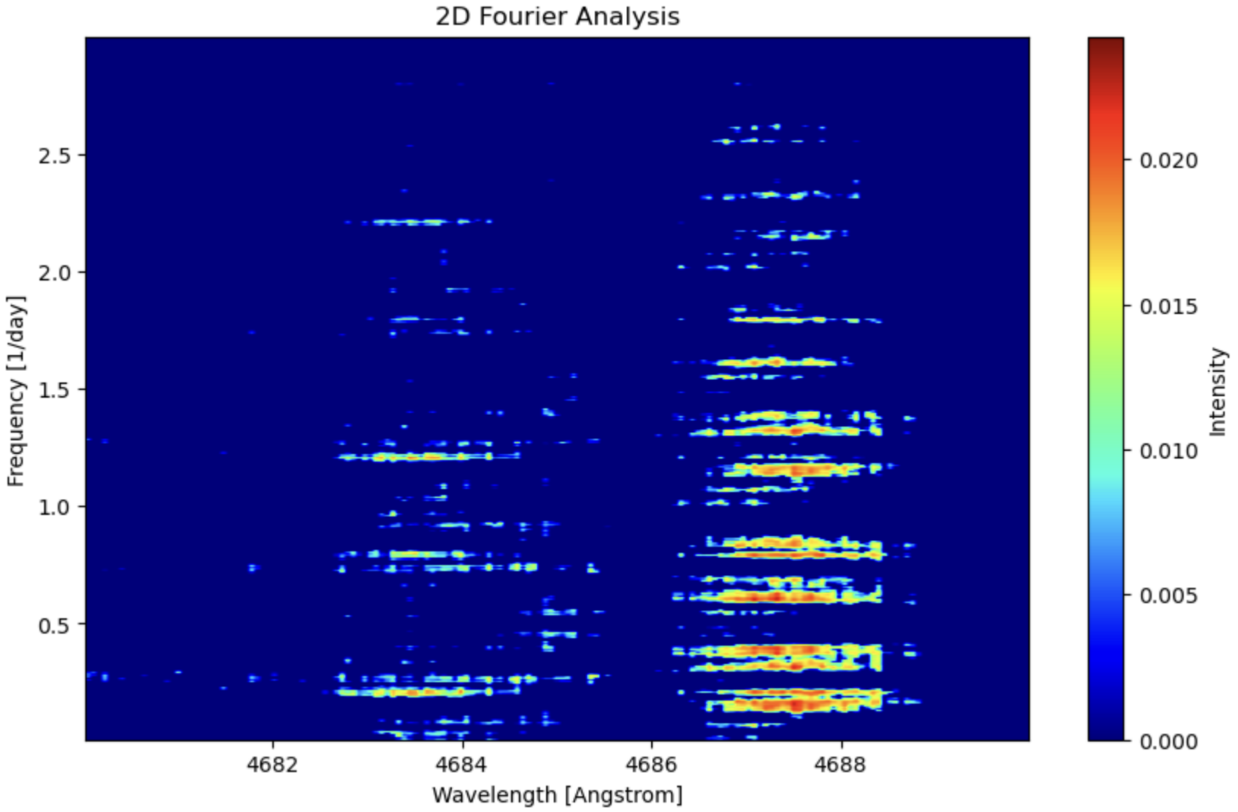

Fig. 67. Fourier 2-D of He II 4686 with a threshold based on the mean noise.

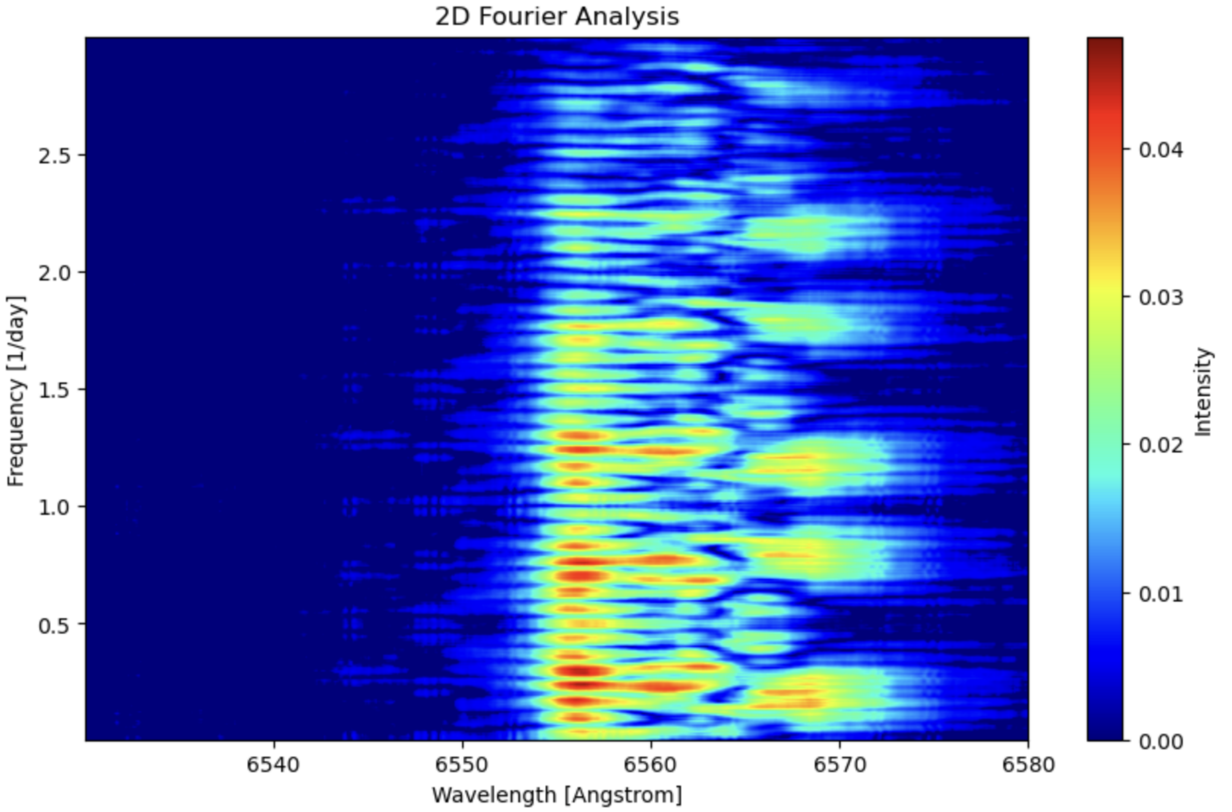

Fig. 68. Fourier 2-D of Hα with a threshold based on the mean noise.

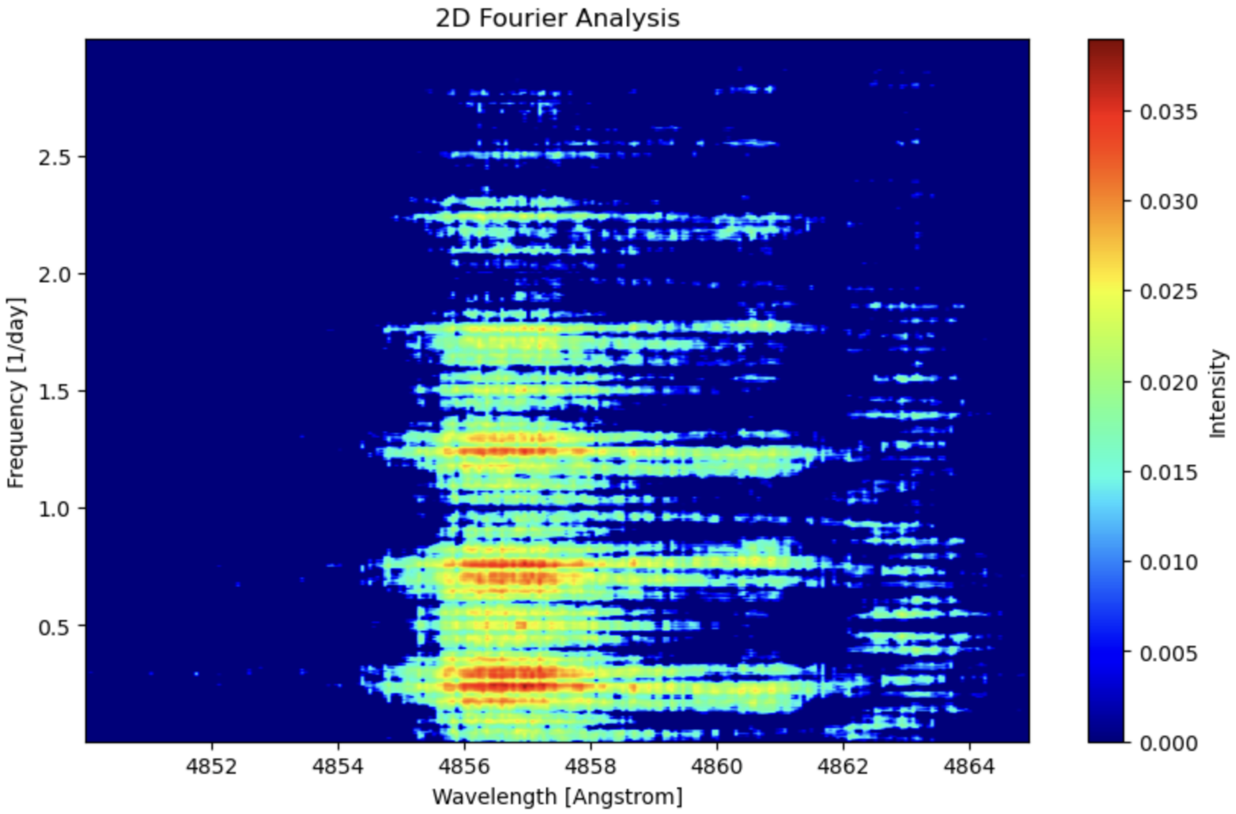

Fig. 69. Fourier 2-D of Hβ with a threshold based on the mean noise.

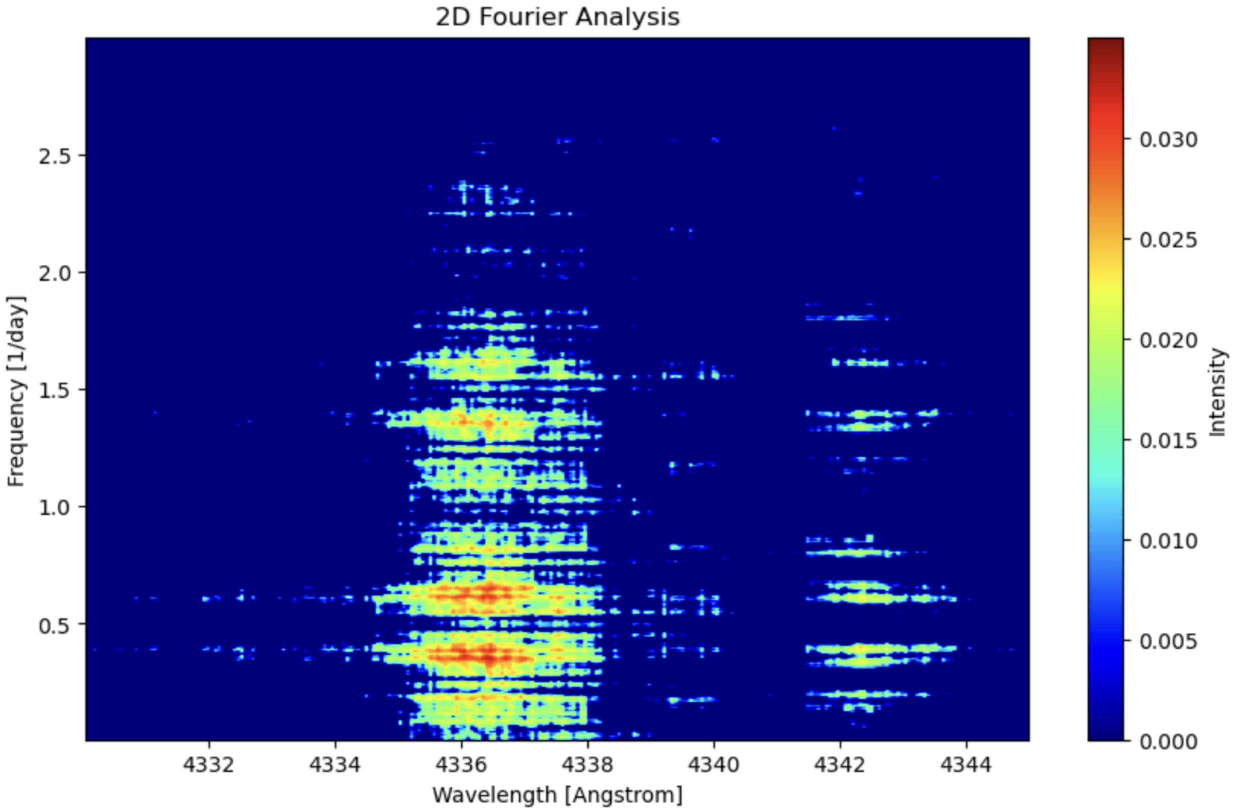

Fig. 70. Fourier 2-D of Hγ with a threshold based on the mean noise.

3.2.5 Rotational velocity

Finally it is possible to estimate the rotational speed of the star. To this end, we use the mean profiles of some specific metal lines and realize a Fourier transform, depending on the wavelength and not the time in this instance. We select metal lines isolated from other spectral features and well defined. In this case, C IV 5812 and O III 5592 were selected. The choice of metal lines is important as those features are less affected by pressure broadening due to the Stark effect than H or He lines.

This result in an empiric Fourier transform of the line profile that can be compared with a theoretical Fourier transform of the rotational broadening function. The broadening function of course depends on the value of $v\sin(i)$. We then adjust the projected rotational velocity until we find a good fit to the empirical Fourier transform. In our case, the best-fit values of the $v\sin(i)$ is about 115 km s^{-1} give (see Figs.71 and 72).

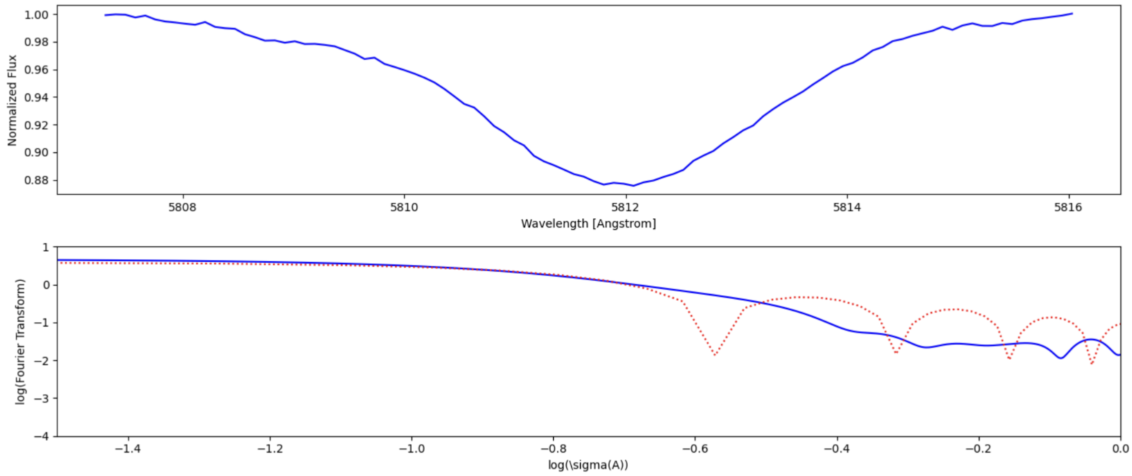

Fig. 71. Above: the normalized flux of C IV 5812; bellow: in blue the Fourier transform of the mean line profile, in red the Fourier transform of the theoretical rotational broadening function for C IV 5812.

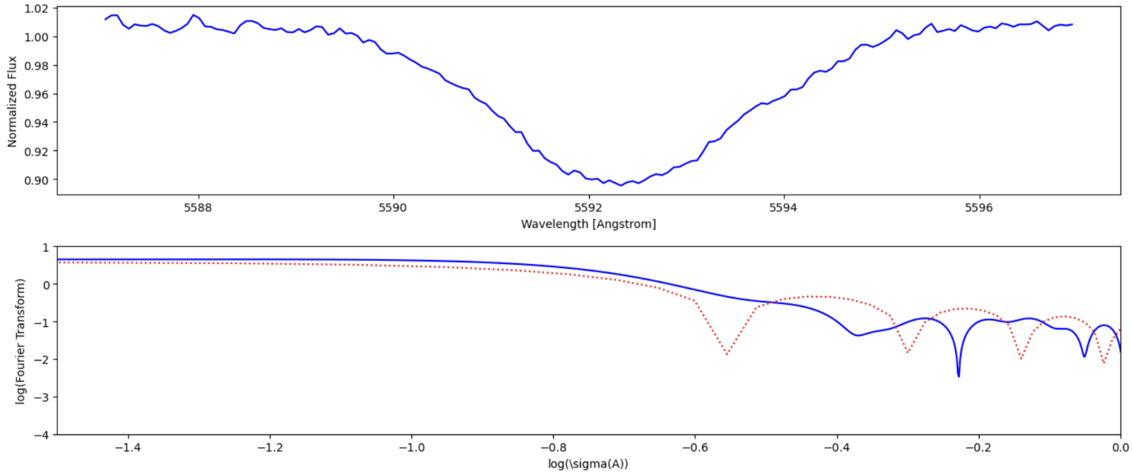

Fig. 72. Above: the normalized flux of O III 5592; bellow: in blue the Fourier transform of the mean line profile, in red the Fourier transform of the theoretical rotational broadening function for O III 5592

3.3 Night of the 27-28 July 2021

During that night, an interesting feature appeared in the wind spectral lines: as the night went on, a discrete absorption component slowly drifting blueward could be observed in the blue wing of He I and HI lines. This was more clearly observed in the line He I 5876. Taking the blue curve as a reference for what the line looks like during the other nights, the migrating absorption component can clearly be seen (Fig. 73).

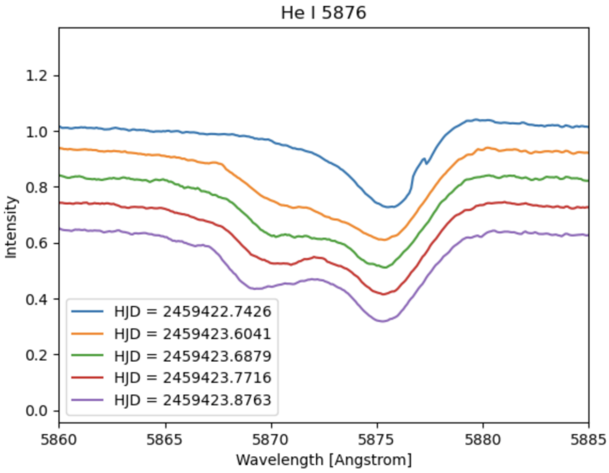

Fig. 73. He I 5876 during the night of 26-27 July 2021 in blue for reference, the other color correspond to the blueshift during the night of 27-28 July 2021.

In Table 3.4, the position of the additional blue absorption bump He I 5876 and Hβ can be seen shifting to the blue during the night.

Table 3.4: Temporal evolution of the center of the discrete absorption component on the night of 27-28 July 2021

HJD-2459000	center of Hβ [Å]	center of He I 5875 [Å]
423.6041	4857.217	5870.578
423.6250	4857.097	5870.360
423.6460	4857.147	5870.256
423.6669	4857.258	5870.390
423.6879	4856.691	5870.067
423.7088	4857.046	5869.982
423.7297	4856.805	5870.086
423.7507	4856.760	5869.887
423.7716	4856.669	5869.993
423.7925	4856.557	5869.833
423.8135	4856.312	5869.662
423.8344	4856.628	5869.522
423.8553	4856.507	5869.342
423.8763	4856.106	5869.317

Coincidentaly, this shift corresponds to the strong dip seen at the beginning of the TESS Sector 41 photometric observations that we described in the photometric section.

Chapter 4

Discussion and conclusion

4.1 Discussion

The results of this study have shed new light on the photometric and spectroscopic variability of the prototypical O7.5 supergiant HD192639. Five epochs of TESS photometry and over 100 TIGRE spectra were analyzed in this work, including the study of the behavior of multiple lines. To highlight and understand the new information brought by our study, we adopt a dual approach. First, we consider each result of our work individually to understand their implications, but also to identify potential flaws. Then we consider all results together to obtain a global view and gain enough hindsight to distinguish a possible pattern. Of course, one must remain careful in doing so: while it is interesting to propose a scenario, it is even more important to be aware of its limitations.

The first dataset analyzed was the photometric data. After Fourier analysis, no frequency stands clearly out compared to the noise threshold we had adopted. The noise here is not only instrumental, but is actually dominated by so-called red noise which is commonly observed in high-precision spaceborne photometry of massive stars. However, as indicated in section 3.1.2, all those periodograms present one of their strongest peaks close to 0.21 day^{-1}. Whilst the amplitudes of those peaks remain below the significance threshold, their repetition likely indicates that they represent a weak signal of a real phenomenon. Beside this potentially interesting frequency, another important result of the TESS photometry is the important dip in magnitude seen at the beginning of Sector 41. This event was more extreme, both in depth ($\sim 0.05\,\mathrm{mag}$) and in duration (about 2 days), than the variations seen most of the time in the light-curve of HD192639. By chance, the date of this dip corresponded to the time at which the spectroscopic data were collected with TIGRE.

The spectroscopic dataset results provide a wealth of information. Their interpretation requires us to keep in mind that the different lines sample different parts of the stellar atmosphere. To analyze the spectra, we used various techniques to extract different quantities such as the TVS and 2-D Fourier periodograms. We further measured the radial velocities of the spectral lines and determined the projected rotational velocity of the star.

The TVS figures (Figs. 45 to 54) show two distinct tendencies. The first five figures, corresponding to the photospheric lines He II 4200-4542-5412, Si IV 6701 and the interstellar feature Ca II 3933, don't show any genuine line-profile variability. At most, small occasional isolated peaks off the line center by several Åcan be attributed to cosmic rays. The absence of strong variations in the interstellar line is of course expected, but this line was included as a consistency check. Because our spectroscopic data sample various timescales (from hours to days and weeks), the absence of variations in the He II and Si IV lines is highly significant. On the shorter timescales, it indicates that non-radial pulsations are unlikely to play a dominant role in the variations of HD192639. On the timescales of days and weeks, it indicates that HD192639 is probably not a spectroscopic binary.

The TVS of the other five lines, Hα, Hβ, Hγ, He I 5876 and He II 4686, shows clear and distinct variability around each of those lines. The variability in these lines is well above the empirically evaluated significance threshold. Their variability concerns both emission and absorption parts of the line profiles. The supergiant HD192639 has a stellar wind that is sufficiently dense that these line profiles are heavily impacted by the presence of an extended circumstellar environment. The strong variability of these lines contrasts with the constancy of the 'pure' photospheric lines and thus reflects the changing conditions inside the stellar wind.

Considering the radial velocities of the photospheric lines, we first notice, as expected, that the radial velocity of the four photospheric lines varies more than those of the interstellar Calcium line. That being said, those variations remain rather small ,variation of amplitude in the order 10 km s^{-1} compared to the radial velocity of a massive star that can be above 1000 km s^{-1}. This small range argues against HD192639 being a short-period spectroscopic binary. Whilst some small part of these variations could stem from contamination by emission formed in the wind, most of it probably arises in the photosphere as a result of either low-amplitude pulsations, turbulent motion in the atmosphere (macro-turbulence), or rotational modulation due to brightness spots. The Fourier analysis of these radial velocities showed multiple peaks in the low frequency domain, some around 0.21 day^{-1}, that is at the frequency seen in the photometric data. This could hint at some (pseudo-)periodic phenomenon responsible for both phenomena. We will return to this point below. Unfortunately, because of their line profile being more complex than simple absorption or emission, no radial velocity measurement can be done on the wind lines.

Regarding the stellar wind lines, all of them display that same 0.21 day^{-1} frequency in their 2D periodogram. This frequency is, this time, even more easily distinguished. The stronger signature of this feature in the wind lines than in the photometry probably indicates that this frequency mostly reflects a phenomenon taking place in the wind. Indeed, the continuum emission which dominates by far the spectral band of the TESS photometry arises from the photosphere, whereas the Hα, Hβ, Hγ, He I 5876 and He II 4686 lines form at least partially inside the wind and are highly sensitive to the presence of large-scale density or velocity structures in the stellar wind.

Our results show that, while not always easily distinguished, 0.21 day^{-1} appears to be a meaningful frequency for HD192639. This corroborates the previous results of Rauw, G. and Vreux, J.-M. (1998) and Rauw, G., Morrison, N. D., et al. (2001), who reported a period of 4.76 days. Given that Rauw, G. and Vreux, J.-M. (1998) and Rauw, G., Morrison, N. D., et al. (2001) had the same period result, this signal seems stable over more than 20 years. Hence this timescale likely reflects a stable clock of the star. In light of our results, the fact that Markova, N. et al. (2005) did not detect this frequency can probably be explained by their sampling being too scarce. Since binarity does not seem to be the most obvious candidate for the clock, the next best scenario is rotation. Assuming that it corresponds to the stellar rotation period, the large-scale structure in the wind would have to be rooted in some way in the photosphere. While we cannot completely dismiss the possibility of a moderate global magnetic field confining the wind to the magnetic equator of the star, Petit, V. et al. (2019) did not find any spectropolarimetric signature of a strong dipolar magnetic field for HD192639. Hence, the probability that there would be a dipolar magnetic field strong enough to significantly confine the wind is low. A viable alternative scenario would then be bright localized magnetic spots. Such features would remain undetected with current spectropolarimetric techniques, but at the same time they could alter the radiative driving in a way sufficient to trigger large-scale density structures in the wind (so-called CIRs).

If we now consider the various results together, we must first come back to the dip event that was seen in the light-curve of Sector 41 and observed simultaneously in spectroscopy. In fact, we notice that the dip corresponds to a specific variation in the profiles. During that event, the observed profiles of the stellar wind lines displayed a blue-ward moving discrete absorption feature. This is especially prominent in the He I 5876 line, but also affects other wind lines (except He II 4686). One possibility to explain the photometric dip is absorption (actually scattering) of stellar light by a volume of higher density gas crossing our line of sight towards the star. The shape and motion of the discrete extra absorption seem to support this idea.

This extreme dip event seems transient, as only Sector 41 presents such a strong feature, or at least the "full dip" repetition period should be longer than one month, given that it does not repeat itself within a single Sector and not even in any of the other sectors. To determine which scenario is right and what is the recurrence time of such events, a much longer observation period would be needed.

Finally, we must consider the possible mechanism behind that higher density gas cloud responsible for the dip event in Sector 41. Given the timescale and the depth of this dip, it is clearly more likely to correspond to a large-scale structure in the wind than to a small-scale inhomogeneity. This feature could reflect an extreme case of the above-described CIRs or it could reflect a sporadic ejection of higher density material (an eruption) taking place over a fraction of the stellar surface. The blueward motion of the spectral absorption feature associated with this dip indicates that the cloud was in motion towards the observer. The fact that the dip did not reappear (at least not with the same amplitude) hints at the dissipation of the cloud. This and the motion towards us favor a transient mass ejection as the explanation of the event.

4.2 Conclusion

This study has revisited the variability of HD 192639 using photometric and spectroscopic data, including several TESS sectors and TIGRE spectra. As previously found by Rauw, G. and Vreux, J.-M. (1998) and Rauw, G., Morrison, N. D., et al. (2001), a period of 4.76 day, corresponding to the frequency 0.21 day^{-1}, can be detected. While not always above the significance threshold, its repeated occurence denotes its importance. This study shows that this period is constant over a long timescale (at least two decades).

The wind-sensitive lines show clear and significant line-profile variability, reaffirming the presence of dynamic structures in the stellar wind. The photospheric lines, in contrast, show only stochastic fluctuations without consistent periodic modulation, which argues against a strong magnetic field or regular pulsational driving. All the results also tend to undermine the theory of a binary.

The use of the two different thresholds in the 2D Fourier analysis could be refined further in order to generalize their use in similar massive star studies by testing and improving the relation between the TVS and the 99% significance level. The mean noise threshold, while a bit crude is simple to implement. The TVS scaling threshold is an innovative idea and if well refined, other similar studies could greatly benefit from this.

One particularly intriguing finding was the detection of a blueward drifting discrete absorption feature during the night of July 27–28, 2021, coinciding with a photometric dip. This suggests a transient event within the stellar wind, potentially caused by localized density enhancements, asymmetric structures, or an exceptional event. Long-term photometric observation would be necessary to at least confirm or infirm the possibility of a repetitive event with a long period of repetition. The detection of other dips could allow a more focused study about them to better understand the underlying processes. However, such studies would be essentially a bet as nothing tends to show that it is not a one time exceptional event.

While similar studies could indeed improve our understanding of massive stars, what is most urgently needed, in the case of HD192639 is gathering UV observations. As this star emits most of its light in that domain, those observations would be invaluable. Of course, this need for UV data remains valid for all massive stars as the lack of a large dedicated and sensitive UV facility in the last years impedes our understanding of them.

Overall, this thesis reinforces the idea that massive star winds are complex. Future studies, especially those capable of detecting weak magnetic fields or performing high-resolution 3D modeling of the stellar wind, may further illuminate the nature of HD 192639's variability.

Bibliography

Cantiello, M. and Braithwaite, J. (2011). “Magnetic spots on hot massive stars”. In: A&A 534, A140. DOI: 10.1051/0004-6361/201117512. URL: https://doi.org/10.1051/0004-6361/201117512.

Cranmer, S. R. and Owocki, S. P. (1996). “Hydrodynamical Simulations of Corotating Interaction Regions and Discrete Absorption Components in Rotating O-Star Winds”. In: The Astrophysical Journal 462, p. 469. DOI: 10.1086/177166. arXiv: astro-ph/9508004 [astro-ph].

ud-Doula, A. et al. (2023). “3D MHD models of the centrifugal magnetosphere from a massive star with an oblique dipole field”. In: Monthly Notices of the Royal Astronomical Society 520.3, p. 3947. ISSN: 1365-2966. DOI: 10.1093/mnras/stad345. URL: http://dx.doi.org/10.1093/mnras/stad345.

Fullerton, A. W., Gies, D. R., and Bolton, C. T. (1996). “Absorption Line Profile Variations among the O Stars. I. The Incidence of Variability”. In: The Astrophysical Journal Supplement 103, p. 475. DOI: 10.1086/192285.

Gavin, H. P. (2013). “The Levenberg-Marquardt method for nonlinear least squares curve-fitting problems c ©”. In: URL: https://api.semanticscholar.org/CorpusID:5708656.

González-Pérez, J. N. et al. (2022). “Eight Years of TIGRE Robotic Spectroscopy: Operational Experience and Selected Scientific Results”. In: Frontiers in Astronomy and Space Sciences 9, p. 912546. ISSN: 2296-987X. DOI: 10.3389/fspas.2022.912546. URL: https://www.frontiersin.org/journals/astronomy-and-space-sciences/articles/10.3389/fspas.2022.912546.

Harries, T. J. (2000). “Synthetic line profiles of rotationally distorted hot-star winds”. In: Monthly Notices of th
315.4, p. 722.

Hawcroft, C. et al. (2021). “Empirical mass-loss rates and clumping properties of Galactic early-type O supergiants”. In: A&A 655, A67. DOI: 10.1051/0004-6361/202140603. URL: https://doi.org/10.1051/0004-6361/202140603.

Heck, A., Manfroid, J., and Mersch, G. (1985). “On period determination methods”. In: AAPS 59, p. 63.

Hinkle, K. et al. (2000). “Visible and Near Infrared Atlas of the Arcturus Spectrum 3727-9300 A”. In: Visible and Near Infrared Atlas of the Arcturus Spectrum 3727-9300 A ed. Kenneth Hinkle, Lloyd Walla
-1.

Jenkins, J. M. et al. (2016). “The TESS science processing operations center”. In: Software and Cyberinfrastruc
Society of Photo-Optical Instrumentation Engineers (SPIE) Conference Series 9913, 99133E. Ed. by Gianluca Chiozzi and Juan C. Guzman, 99133E. DOI: 10.1117/12.2233418.

Mannino, G. and Humblet, J. (1955). “Observations spectroscopiques de quelques étoiles Of (I)”. In: Annales d’Astrophysique 18, p. 237.

Marcolino, W. L. F. et al. (2022). “Wind properties of Milky Way and SMC massive stars: empirical Z dependence from <scp>cmfgen</scp> models”. In: Monthly Notices of the Royal Astronomical Society 511.4, p. 5104. ISSN: 1365-2966. DOI: 10.1093/mnras/stac452. URL: http://dx.doi.org/10.1093/mnras/stac452.

Markova, N. et al. (2005). “Bright OB stars in the Galaxy - II. Wind variability in O supergiants as traced by H”. In: A&A 440.3, p. 1133. DOI: 10.1051/0004-6361:20041774. URL: https://doi.org/10.1051/0004-6361:20041774.

Martins, F. et al. (2015). “The MiMeS survey of magnetism in massive stars: CNO surface abundances of Galactic O stars”. In: A&A 575, A34, A34. DOI: 10.1051/0004-6361/201425173. arXiv: 1411.4420 [astro-ph.SR].

Nazé, Y., Rauw, G., and Gosset, E. (2021). “Red noise and pulsations in evolved massive stars”. In: Monthly Notices of the Royal Astronomical Society 502.4, p. 5038. ISSN: 0035-8711. DOI: 10.1093/mnras/stab133. eprint: https://academic.oup.com/mnras/article-pdf/502/4/5038/36432776/stab133.pdf. URL: https://doi.org/10.1093/mnras/stab133.

Petit, V. et al. (2019). “The MiMeS survey of magnetism in massive stars: magnetic properties of the O-type star population”. In: Monthly Notices of the Royal Astronomical Society 489.4, p. 5669. ISSN: 1365-2966. DOI: 10.1093/mnras/stz2469. URL: http://dx.doi.org/10.1093/mnras/stz2469.

Rauw, G., Morrison, N. D., et al. (2001). “The spectral variability of HD 192639 and its implications for the star’s wind structure*”. In: A&A 366.2, p. 585. DOI: 10.1051/0004-6361:20000106. URL: https://doi.org/10.1051/0004-6361:20000106.

Rauw, G. and Vreux, J.-M. (1998). “Line profile variability in the spectrum of the O(f) supergiant HD 192639”. In: Astronomy and Astrophysics 335, p. 995.

Shull, J. M. and Danforth, C. W. (2019). “Distances to Galactic OB Stars: Photometry versus Parallax”. In: The Astrophysical Journal 882.2, p. 180. DOI: 10.3847/1538-4357/ab357d. URL: https://dx.doi.org/10.3847/1538-4357/ab357d.

TESS Instrument Handbook Version 0.1 (Draft of 6 December 2018) (Last accessed 14 november 2024). https://archive.stsci.edu/missions/tess/doc/TESS_Instrument_Handbook_v0.1.pdf.

TESS NASA Website (Last accessed 14 november 2024). https://heasarc.gsfc.nasa.gov/docs/tess/observing-technical.html.